Contributions to Mineralogy and Petrology (2024) 179:58
https://doi.org/10.1007/s00410-024-02134-z

ORIGINAL PAPER

Experimental insights into the mineralogy and melt-rock reactions produced by lunar cumulate mantle overturn

J. L. Scholpp[1] · N. Dygert[1]

Received: 17 November 2023 / Accepted: 15 April 2024 / Published online: 13 May 2024

Abstract

Hybridization of the lunar mantle during the overturn (sinking) of Fe- and Ti–rich ilmenite-bearing clinopyroxenite cumulates (IBC) in the lunar interior is called upon to explain the high TiO_2 abundances of lunar basalts. Chemical reactions that occur after juxtaposition of IBC and mantle peridotite are poorly constrained. We experimentally investigated these reactions in experiments that adjoin an IBC glass against presynthesized dunite in a reaction couple at temperatures of 1100–1300 °C and pressures of 0.5–2.02 GPa for 0.33–31.66 h. These conditions produced experiments near to well above the solidus temperature of the IBC. Near solidus experiments produce garnet in the IBC at 2 GPa. Supersolidus experiments exhibit dissolution of olivine material into the IBC melt and the formation of clinopyroxene at the IBC melt-dunite interface. Dunite dissolution is attributed to the olivine undersaturated composition of the IBC melt. In both near- and supersolidus experiments, compositional variations produced by solid-state diffusion across the IBC melt-dunite interface are observed. When pressure increases, temperature decreases, or IBC melts become closer to olivine saturation, dissolution slows, and the effects of solid-state diffusion in the dunite become more evident. Similar chemical exchange reactions would occur in the lunar mantle as downwelling IBC and lunar peridotites are juxtaposed by cumulate overturn. Hybridized lunar mantle sources are expected to contain 47–84% normative peridotite and 16–53% IBC. Simple numerical simulations suggest that in addition to dissolution–precipitation reactions, mechanical mixing may be required to produce volumetrically significant hybridized mantle sources over geologically-relevant timescales.

Keywords Mantle Hybridization · Lunar mantle · Overturn

Introduction

The origin and formation mechanisms of lunar mare basalt and picritic glass mantle sources have been debated since analysis of Apollo returned samples revealed that the basalts exhibit variable TiO_2 and REE concentrations with a wide range of Mg#s (Mg# = molar Mg/(Mg + Fe) × 100) (Delano 1986; Haskin and Warren 1991; Shearer et al. 1991, 2015; Shearer and Papike 1993; Papike et al. 1998; Neal 2001). This chemical variation is attributed to the chemical diversity of lunar mantle sources (e.g., Lucey et al. 1998; Giguere et al. 2000; Shearer et al. 2015). Lunar mantle sources may have formed after solidification of a lunar magma ocean (LMO), which would produce layers of mafic cumulates (olivine and then olivine and orthopyroxene) beneath clinopyroxene and ilmenite-bearing cumulates of more evolved residual magma ocean liquids. Despite the mineralogical diversity of these LMO cumulate layers, they individually cannot explain the compositions of many mare basalt sources (Snyder et al. 1992; Elardo et al. 2011; Elkins-Tanton et al. 2011; Lin et al. 2017; Charlier et al. 2018). Thus, a post-LMO solidification mantle hybridization mechanism is invoked to effectively mix shallow and deep magma ocean cumulates to account for the mare basalt and picritic glass chemical compositions (Hess and Parmentier 1995; Singletary and Grove 2008; Thacker et al. 2009; Yao and Liang 2012; Mallik et al. 2019). This work explores processes that control mantle hybridization inferred to produce lunar basalt sources.

Magma ocean crystallization experiments testing a bulk Moon with an lunar primitive upper mantle (LPUM)-like

Communicated by Othmar Müntener.

✉ J. L. Scholpp
jscholpp@vols.utk.edu

[1] Department of Earth and Planetary Sciences, University of Tennessee, Knoxville, USA

(Longhi 2003) composition show consistent trends during magma ocean solidification with olivine as the initial crystallizing phase (Elardo et al. 2011; Elkins-Tanton et al. 2011; Lin et al. 2017; Charlier et al. 2018; Rapp and Draper 2018). This is followed by olivine (Ol) and orthopyroxene (Opx) as the SiO_2 concentration in the melt increases (Elkins-Tanton et al. 2011; Charlier et al. 2018). At 60–70% crystallization of the magma ocean, high-Ca pyroxene (i.e., pigeonite and augite) and plagioclase (i.e., anorthite) become saturated. Since plagioclase is less dense than the melt from which it crystallized, it will float to the top of the LMO and form an anorthosite crust (Wood et al. 1970; Walker and Hays 1977; Dygert et al. 2017). Ilmenite ($FeTiO_3$) and possibly other Fe-Ti oxides (e.g., Ulvöspinel ($TiFe_2O_4$), Armalcolite ($(Mg,Fe)Ti_2O_5$)) begin to crystallize at 90–95% magma ocean solidification and likely continue to precipitate until the end of magma ocean solidification (Elkins-Tanton et al. 2011; Lin et al. 2017; Charlier et al. 2018). Although high-pressure crystallization experiments with Taylor Whole Moon (TWM)-like (Taylor 1982) starting compositions have produced garnet as an LMO cumulate (Elardo et al. 2011; Jing et al. 2022; Kraettli et al. 2022), garnet has not been observed in crystallization experiments assuming an LPUM-like bulk Moon composition regardless of the pressure. Thus, if we assume the LMO had an LPUM-like composition, garnet is likely to have been absent from the initial magma ocean cumulates.

Mineral stratification in the post-LMO cumulate mantle is controlled by the phase saturation sequence and phase density due to fractional crystallization of the solidifying LMO. After LMO solidification, the Moon is thought to have had an olivine-rich dunite surrounding the core, harzburgite above the dunite layer, a clinopyroxene- (Cpx) and ilmenite-bearing cumulate (IBC) atop the harzburgite, and an incompatible element enriched (i.e., KREEP- Potassium, Rare Earth Element, and Phosphorous) residual melt region or cumulate near or above the IBC layer, all beneath an anorthosite crust (Snyder et al. 1992; Hess and Parmentier 1995; Elkins-Tanton et al. 2011; Dygert et al. 2017, Rapp and Draper 2018). The late, shallow precipitation of dense IBC produces a gravitationally unstable lunar mantle stratigraphy, with less dense ilmenite-free cumulates beneath the dense IBC (for reference, ilmenite is ~ 4720 kg/m^3, magnesian olivine is ~ 3400 kg/m^3, magnesian orthopyroxene is ~ 3300 kg/m^3 at atmospheric pressure) (Snyder et al. 1992; Hess and Parmentier 1995; Elkins-Tanton et al. 2011; Zhang et al. 2017; Li et al. 2019). Elkins-Tanton et al. (2002) argue the overturn of solidified IBC is unlikely given the viscosities and temperatures of mantle cumulates, and other studies argued it might be inefficient owing to the IBC viscosity (Zhao et al. 2019), but recent studies that account for the low viscosity of ilmenite relative to lunar mantle silicates (Dygert et al. 2016; Tokle et al. 2021), suggest that the gravitationally unstable stratigraphy would have resulted in cumulate overturn (Zhang et al. 2017; Li et al. 2019; Maurice et al. 2024). These recent studies indicate that dense shallow cumulates flow into the deep lunar interior as viscous solids, perhaps after progressive thickening of the IBC layer by downwelling of small scale IBC instabilities into the underlying mantle (Hess and Parmentier 1995; Li et al. 2019). The overturn of IBC into the lunar mantle would juxtapose sinking IBC against deep mafic mantle cumulates, where mechanical mixing or chemical reactions could generate hybridized mantle sources.

Although multiple lunar basalt formation mechanisms have been proposed (e.g., Hubbard and Minear 1975), mantle hybridization is considered a capable mechanism for forming sources of high-Ti lunar basalts and picritic glasses (Ringwood and Kesson 1976; Hess and Parmentier 1995; Wagner and Grove 1997; Van Orman and Grove 2000; Elkins-Tanton et al. 2002). Hybridization is invoked to explain the Ti- and REE-rich compositions of the lunar basalts (relative to mafic cumulates of a lunar magma ocean) and high Mg#s (relative to that estimated for the IBC) (e.g., Singletary and Grove 2008; Grove and Krawczynski 2009; Krawczynski and Grove 2012; Brown and Grove 2015). Previous studies have estimated the composition of the hybridized sources by mixing various proportions of late LMO cumulates and mafic cumulates (Singletary and Grove 2008; Thacker et al. 2009; Yao and Liang 2012; Mallik et al. 2019) and investigated the phase equilibria of the downwelling IBC (Van Orman and Grove 2000; Mallik et al. 2019). While these studies provide a first-order understanding of the starting material and possible end products of the hybridization process, they do not explore the chemical reactions that control the hybridization process.

This study experimentally investigates the chemical reactions that occur during the cumulate overturn as downwelling IBC melts and mushes interact with mafic cumulates. The experiments indicate that the primary processes contributing to hybridization are the dissolution of mafic material and solid-state diffusion between cumulates. The experimental results also constrain metamorphic phase relations in the downwelling IBC, which indicate garnet would form in the lunar mantle during cumulate mantle overturn events.

Methods

Starting materials

Experiments tested the mineralogy and mineral reactions that occurred between dunite representing early lunar magma ocean cumulates and an ilmenite-bearing cumulate (IBC) under supersolidus and near solidus conditions (for

the IBC). The IBC composition in this study represents a late lunar magma ocean cumulate comprising 85% normative hedenbergite clinopyroxene and 15% normative ilmenite (Longhi and Ashwal 1985; Snyder et al. 1992; Hess and Parmentier 1995). The assumed pyroxene composition is an average of LMO-relevant pyroxene compositions NJD-20, HB-1, HB-4 from Dygert et al. (2014), while the assumed ilmenite composition is an average of LMO-relevant ilmenite compositions NJD-22 M, NJD-19 M, NJD-17 M, NJD-15 M from Dygert et al. (2013). Reagent-grade metal oxide and carbonate powders were used to prepare the IBC starting composition. The powders were weighed and ground in a mortar and pestle for 12 h, then decarbonated in a furnace at 800 °C for 24 h. Following the decarbonation, the powder was conditioned at an oxygen fugacity (fO_2) relevant to the lunar mantle, which is close to the iron-wüstite (IW) buffer (Sato 1979; Weitz et al. 1997; Nicholis and Rutherford 2009). The powder was placed in a gas mixing furnace at 800 °C in a gas mixture with subequal volumes of CO_2 and H_2 (Deines 1974) to achieve an fO_2 approximating IW. The IBC cumulate melt has a Ti-, Al-, and Fe-rich composition with an Mg# of 4.96 ± 0.12 (Table 1).

A lunar-relevant mafic cumulate composition represented by a terrestrial dunite was prepared using mineral separates from a mantle xenolith (Dygert et al. 2019). The dunite consists of olivine mineral separates with trace amounts of Opx, Cpx, and minor spinel from the crushed mantle xenolith. The dunite separates were ground in ethanol, dried, and stored in a 200 °C vacuum oven for at least 12 h to drive off adsorbed water. The olivine from the dunite used in reaction experiments has an Mg# of 90.83 ± 0.07 (Table 1.).

Experiments

Experiments were conducted at the University of Tennessee using a 150-ton end-loaded piston cylinder apparatus equipped with a computerized pressure holding system. Assembly designs are similar to those utilized by Morgan and Liang (2005) and Wang et al. (2013). Experiments were run in graphite-lined molybdenum capsules, which were previously demonstrated to approach lunar-relevant value fO_2s near the IW buffer for similarly preconditioned starting materials (Ji and Dygert 2024). Dunite and IBC materials were presynthesized before running the reaction experiments. The IBC materials were heated to 1300 °C at 1 GPa for 2 h and then quenched to a glass. Dunite was annealed at 1200 °C at 1 GPa for 24 h to texturally equilibrate. The presynthesized runs were then sectioned latitudinally, polished, and reaction couples were prepared by juxtaposing the IBC glass against the dunite. Reaction couples were held together using platinum foil and placed in experimental assemblies

Table 1 Starting material compositions (wt%) measured by electron microprobe from this study compared with ilmenite-bearing cumulate compositions from previous studies

	IBC (This Study)		Dunite (This Study)		TiCum (VO&G' 00)	TiCum (M' 19)	TiCum Est (C' 18)
	Avg	σ	Avg	σ			
SiO_2	38.03	0.15	41.42	0.27	41.61	41.90	32.40
TiO_2	6.83	0.10	0.01	0.01	9.10	9.10	12.63
Al_2O_3	6.26	0.08	0.05	0.02	2.80	3.24	5.51
Cr_2O_3	0.26	0.01	0.12	0.01	0.00	0.01	0.03
MgO	0.91	0.02	49.90	0.15	7.50	7.95	4.34
CaO	13.91	0.10	0.20	0.02	8.20	8.48	5.38
MnO	1.05	0.02	0.14	0.01	0.00	0.03	0.40
FeO	31.21	0.09	8.98	0.05	29.60	28.90	39.15
NiO	0.00	0.00	0.40	0.03	0.00	0.00	0.00
Na_2O	0.29	0.02	0.01	0.00	0.00	0.02	0.15
K_2O	0.00	-	0.00	-	0.00	0.02	0.01
Total	98.75	0.23	101.22	0.35	98.81	99.65	100.00
Mg#	4.96	0.12	90.83	0.07	31.11	32.90	16.49

Mg# = (Mg/(Mg + Fe)) × 100

VO&G' 00—Van Orman and Grove (2000)

M' 19—Mallik et al. (2019)

C' 18—Charlier et al. (2018)

TiCum Est—Estimated composition of the ilmenite-bearing cumulate from Charlier et al. (2018) determined with the modal mineral abundances and mineral compositions from crystallization experiments (LPUM/02–3 gl). Composition assumes 80% floation of plagioclase and quartz based on the findings of the study

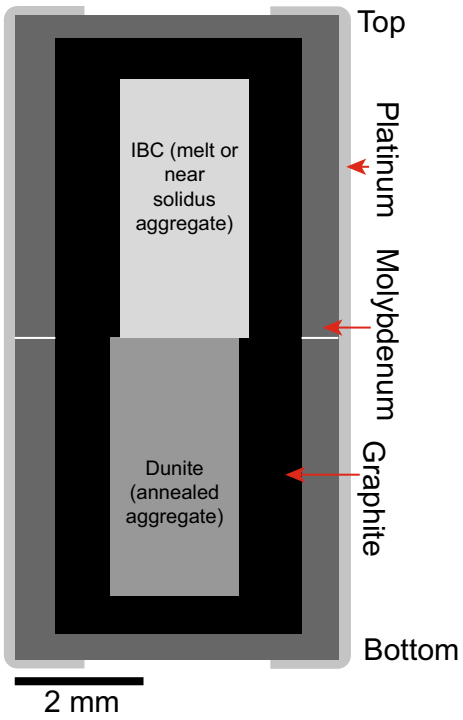

Fig. 1 Schematic illustrating assemblies used in near solidus and melt-rock reaction experiments utilized in this work. IBC refers to half of the reaction couple with the ilmenite bearing cumulate composition

composed of crushable MgO spacers within a graphite resistance heater and Pyrex sleeve, using outer NaCl salt sleeves as a confining material, with the IBC glass above the dunite (Fig. 1). No pressure correction was applied. Temperature was monitored using calibrated D-type W–Re thermocouples, and no emf correction was applied.

Eight of the experiments were run in a three-step, heat-dwell-quench sequence to examine whether a reaction would occur between the halves of the reaction couple (Table 2). These eight experiments were run at temperatures between 1100 and 1300 °C at pressures between 0.55 and 2.02 GPa for durations of 20 min to 24 h. One experiment (MRx#13) was run as a five-step, heat-dwell-cool-dwell-quench sequence to examine the effects of dunite dissolution on a hybridized cumulate (Table 2). This experiment was run at 2.02 GPa and had an initial 6 h dwell period at 1300 °C, followed by a 1 h and 40 min cooling period, which cooled the experiment at a rate of 1 °C/min. The cooling period decreased the temperature to 1200 °C, and the experiment dwelled at this temperature for 24 h before quenching (Table 2).

Analysis of run products

Run products were extracted from assembles, mounted in epoxy resin, cut lengthwise with a low-speed saw, and

Table 2 Starting materials and run conditions

Experiment	Starting Materials	P (GPa)	T (°C)	Duration (hr)	Temperature Path (°C)	Run Products	Assimilation	Group
MRx#1	IBC + Dunite	2.02	1200	6	0 (70 °C/min) ➔ 1200 (6 h) ➔ Quench	Garnet + Cpx + Fe-Ti Oxide^	No	N/A
MRx#3	IBC + Dunite	1.99	1100	6	0 (70 °C/min) ➔ 1100 (6 h) ➔ Quench	Garnet + Cpx + Ilmenite + Ulvospinel	No	N/A
MRx#5	IBC + Dunite	0.55	1200	6	0 (70 °C/min) ➔ 1200 (6 h) ➔ Quench	Glass + Cpx	Yes	A
MRx#8	IBC + Dunite	2.02	1150	24	0 (70 °C/min) ➔ 1150 (24 h) ➔ Quench	Garnet + Cpx + Ilmenite	No	N/A
MRx#9	IBC + Dunite	0.55	1200	0.33	0 (70 °C/min) ➔ 1200 (0.33 h) ➔ Quench	Glass + Cpx*	Yes	A
MRx#10	IBC + Dunite	0.55	1200	24	0 (70 °C/min) ➔ 1200 (24 h) ➔ Quench	Glass + Cpx	Yes	A
MRx#11	IBC + Dunite	0.55	1100	24	0 (70 °C/min) ➔ 1100 (24 h) ➔ Quench	Cpx + Ulvospinel + glass	No	B
MRx#12	IBC + Dunite	2.02	1300	1	0 (70 °C/min) ➔ 1300 (1 h) ➔ Quench	Cpx + Fe-Ti Oxide^	Yes	A
MRx#13	IBC + Dunite	2.02	1300–1200	31.66	0 (70 °C/min) ➔ 1300 (6 h) ➔ (-1 °C/min)➔ 1200 (24 h) ➔ Quench	Glass + Cpx	Yes	N/A

^FeTi-Oxide indicates that High-Z phases were present in the reaction products; however, the grain size of the phases made analysis impossible

*Cpx indicates that a silicate crystals were present in the reaction products; however, the grain size of the crystals made analysis impossible

Group A supersolidus experiements exhibit significant evidence of dunite dissolution

Group B supersolidus experiments lacked clear evidence of dissolution

polished. Imaging and mineral chemistry measurements were conducted using the Cameca SX100 electron probe microanalyzer (EPMA) at the University of Tennessee, Knoxville. For quantitative wavelength dispersive spectroscopy (WDS) mineral analyses, operating conditions were 15 kV and 30 nA, with a spot size of 1 µm. For glass analysis, a defocused 10 µm beam was used, and operating conditions were 15 kV and 20 nA. X-ray counts were measured for 30–40 s on the peak position of each element and 10 s on background. Natural and synthetic standards were used for calibration, and the ZAF matrix correction was applied. X-ray maps of the reaction interface were created with the Phenom XL at the University of Tennessee, Knoxville. For qualitative energy dispersive spectroscopy (EDS) mapping, operating conditions were 15 kV and 30 nA, under a 1 Pa vacuum, with a spot size of 2 µm. The count time per spot was set to 20 ms for variably sized areas of interest with a resolution of 1024 × 1024 pixels. Since the mapping area and resolution determine the point density, the point density ranges from 0.1 µm to 2 µm among maps.

Results

Experiments juxtaposing the IBC glass and dunite in this study are presented in three groups: (1) near solidus experiments, (2) supersolidus dunite dissolution experiments, and (3) a dunite dissolution-solidification experiment. (Table 2). In all cases, the dunite half of the reaction couple was below its melting temperature; near solidus and supersolidus refer to the behavior of the IBC side of the reaction couple. Near solidus experiments are classified as experiments that contain ≤ 1% melt in the IBC half of the couple, while supersolidus experiments have > 30% melt in the IBC half of the couple. The melt proportion was determined using volumetric estimates from chemical maps where the minerals and melt are easily distinguished. ImageJ was the image processing software used for these calculations. Results for each experimental group are discussed separately. All chemical data collected from each experiment are reported in the Electronic Supplement.

Near solidus experiments

Products and growth textures

Experiments MRx#1, MRx#3, and MRx#8 were run under near solidus conditions (Table 2), with trace amounts of a low-degree interstitial melt in the IBC side of the reaction couple. These experiments produce Cpx and garnet with variable amounts of Fe-Ti oxides (i.e., ulvöspinel and ilmenite) throughout the IBC side of the reaction couple (Figs. 2a). Growth textures of Cpx and garnet crystals are often subhedral. Ilmenite and ulvöspinel exhibit subhedral and anhedral growth textures. Garnets often contain inclusions of Cpx and Fe-Ti oxides and are difficult to distinguish from Cpx in BSE images owing to the similar average atomic number of the minerals in this system (Fig. 2b). Ulvöspinel and ilmenite often form as inclusions within garnet and in the interstitial space between garnet and Cpx crystals. Trace amounts of low-degree interstitial melt are present along the edge of the IBC material (MRx#8) (Fig. 2a) and between crystals (MRx#1) (Fig. 2d). Garnet represents ~ 19% of the IBC half of the reaction couple in these high-pressure experiments, while Cpx and Fe-Ti oxides represent ~ 78% and ~ 3% respectively. Low-degree interstitial melt makes up < 1% of the material in the IBC side of experiments MRx#1 and MRx#8, while MRx#3 appears to be free of interstitial melt.

A diffusive exchange layer ~ 10–60 µm thick is present around the original interface (Fig. 2d and Supplemental Figs. 1 & 2). The thickness of the reactive layer interface appears to increase with time (Table 3). It should be noted that fractures often form at the interface between halves of the experimental reaction couples, making accurate measurements difficult within and near the reaction boundary. Thus, the dunite boundary thicknesses for MRx#3 and MRx#8 reported in Table 3 represent minimum estimates as material may have been lost during fracture formation, mounting, and polishing.

Phase chemistry

Clinopyroxenes from near solidus experiments have Al & Ti–rich hedenbergitic compositions (Fig. 3a). Garnets produced in the experiments have high almandine (Alm) and grossular (Gro) components with almost no pyrope component (Fig. 4). Garnet from MRx#1 is more grossular normative than garnets from MRx#3 and MRx#8. This may be related to the higher temperature of the MRx#1 experiment. Ulvöspinel and ilmenite were observed in MRx#3; however, ulvöspinel was not observed in MRx#8. High-Z phases are present in MRx#1 and are likely Fe-Ti oxides; however, these phases are typically < 3 µm across, so single-phase analysis was impossible. Low-degree interstitial melt in MRx#1 and MRx#8 is TiO_2 and FeO enriched, but SiO_2, Al_2O_3, Cr_2O_3, and MgO depleted relative to the initial IBC composition (Table 4).

Clinopyroxene crystals that form on the boundary between the dunite and IBC sides of the reaction couple typically have more augitic compositions and plot separately from Cpx that form within the IBC side and far from the boundary (Figs. 2c, d, and 3a). Olivine within the dunite side is more fayalite (Fa) normative at the boundary (Figs. 2b, c), consistent with diffusive chemical exchange between the dunite and IBC. Considering the width of the dunite boundary layer (~ 30 µm) and the fact that its

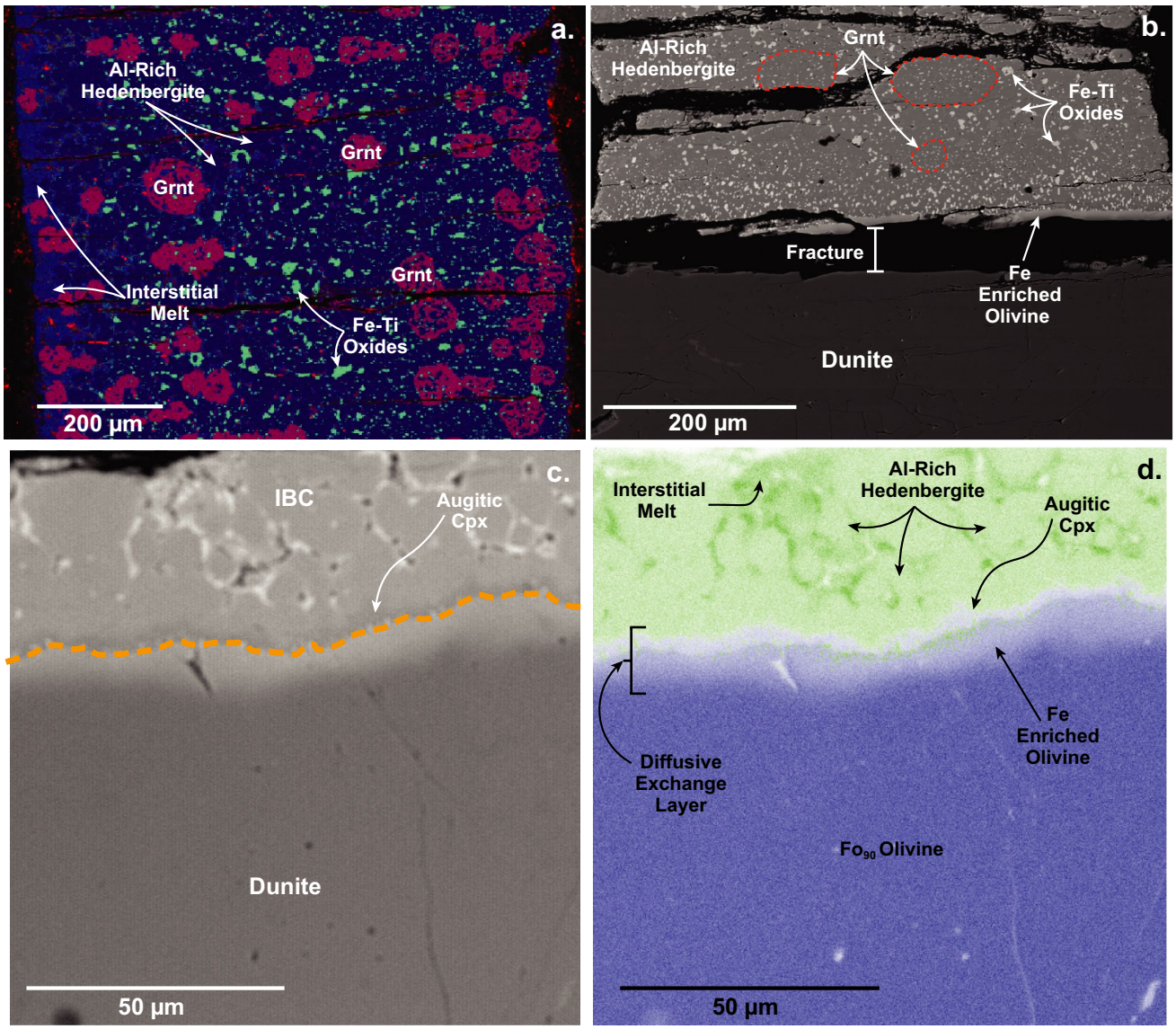

Fig. 2 Representative BSE images and elemental maps highlighting minerals and reactions produced in near solidus experiments. **a** False color image of the IBC half of the reaction couple in MRx#8, showing garnet (red), clinopyroxene (dark blue), Fe-Ti oxides (green), and Ti- and Fe-rich low degree interstitial melt on the left side of the experiment (lighter blue). **b** Backscatter electron image of near solidus experiment MRx#3 showing crystalline features in IBC half of the reaction couple, and diffusive exchange boundary at the IBC-dunite interface. The IBC formed Al-rich hedenbergite, garnet (Grnt) (outlined in red), and Fe-Ti oxides. Boundary reactions observed in MRx#1 are shown in (**c**) and (**d**). **c** Backscatter electron image of the IBC-dunite reaction interface (orange dashed line). Augitic Cpx that formed via diffusive exchange is labeled. **d** Combined Fe (green) and Mg (blue) false color elemental map of the interface showing the diffusive exchange of Fe and Mg. This chemical exchange resulted in the formation of fayalitic olivine and augitic Cpx (light blue and gray-blue respectively in the elemental map)

width increases with experimental duration suggests that it is the product of solid-state diffusive exchange across the reaction couple. As the layer is relatively thin, it is unlikely that the dunite significantly influences the composition of minerals within the IBC side beyond a similarly thin boundary layer adjacent to the dunite. This also indicates that the average pyroxene and garnet compositions in near solidus experiments represent the equilibrium phase compositions within the IBC at the P–T conditions of the given experiment.

Supersolidus experiments

Supersolidus experiments MRx#5, MRx#9, MRx#10, MRx#11, and MRx#12 are divided into group A (MRx#5, MRx#9, MRx#10, and MRx#12) and group B (MRx#11).

Table 3 Interface dissolution and exchange measurements from melt-rock reaction experiments

Experiment	P (GPa)	T (°C)	Duration (hr)	Dunite Diffusion Boundary Thickness (μm)			Dissolution distance (μm)			Estimated Dissolution Propogation (m^2/s)	
				n	Avg	σ	n	Avg	σ	Est	σ
MRx#1	2.02	1200	6	6	10	0.36	–	N/A	–	N/A	–
MRx#3	1.99	1100	6	6	10	1.01	–	N/A	–	N/A	–
MRx#5	0.55	1200	6	–	N/A	–	6	313	50.24	1.45E-14	2.33E-15
MRx#8	2.02	1150	24	6	16	4.40	–	N/A	–	N/A	–
MRx#9	0.55	1200	0.33	–	N/A	–	6	30	79.62	2.51E-14	5.00E-15
MRx#10	0.55	1200	24	6	14	7.67	6	394	6.00	4.56E-15	9.22E-16
MRx#11	0.55	1100	24	6	5	1.41	–	N/A	–	N/A	–
MRx#12	2.02	1300	1	6	6	1.77	6	86	15.83	2.38E-14	4.40E-15
MRx#13	2.02	1300–1200	31.66	6	24	4.28	7	201	18.97	N/A	–

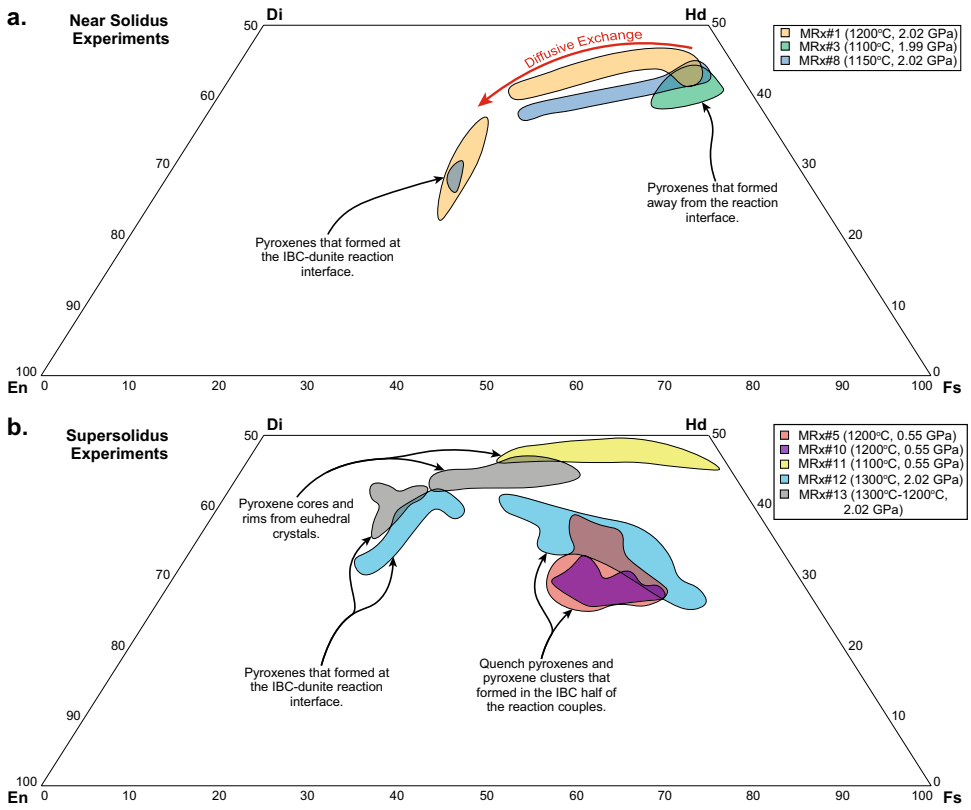

Fig. 3 Pyroxene compositions from melt-rock reaction experiments projected as components. **a** Pyroxene compositions from near solidus experiments. **b** Pyroxene compositions from supersolidus and dissolution–precipitation experiments. Pyroxenes that formed at the interface plot in separated groups as noted for each experiment (except for MRx#11, as the interface pyroxenes have similar compositions to the most magnesian cores of euhedral pyroxenes). Mineral end-members: Enstatite (En), Ferrosilite (Fs), Diopside (Di), Hedenbergite (Hd)

Group A experiments were run at 0.55 GPa (1200 °C) and 2 GPa (1300 °C), and all exhibit significant evidence of dunite dissolution. The Group B experiment was run at 0.55GPa (1100 °C) and lacked clear evidence of dissolution (Table 2). These experimental groups are discussed separately below.

Group A products and growth textures

Both low-pressure (i.e., 0.55 GPa) and high-pressure (i.e., ~ 2 GPa) experiments produce dunite dissolution (assimilation). Evidence of dunite dissolution is evident in backscatter electron (BSE) images where the interface between the dunite and IBC halves of the reaction couple was always offset into the dunite (Fig. 5a and c). The position of the original polished interface is shown in Fig. 5 by the blue line, and the orange line shows the final position of the interface. The IBC side of the reaction couple exhibits Cpx and/or hybridized melt (i.e., IBC melt that has assimilated dunite material) at the reaction boundary. The IBC side of the reaction couple remained glass-rich

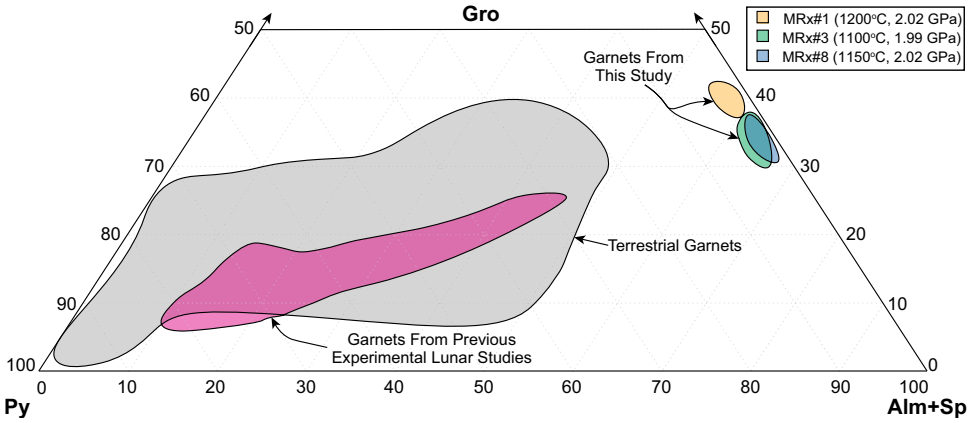

Fig. 4 Garnet compositions from near solidus experiments conducted in this study compared to terrestrial and lunar relevant compositions. Gray shaded terrestrial garnet region represents data compiled by Sun and Liang (2015). Pink shaded lunar garnet region represents experimental garnets from picritic glass multi-saturation experiments, hybridized lunar mantle source experiments, and lunar magma ocean solidification studies (Elkins-Tanton et al. 2003; Draper et al. 2006; Elardo et al. 2011; Krawczynski and Grove 2012; Barr and Grove 2013; Mallik et al. 2019; Kraettli et al. 2022; Jing et al. 2022). Mineral end-members: Almandine (Alm), Spessartine (Sp), Grossular (Gro), Pyrope (Py)

Table 4 Pre-reaction IBC composition compared with post-reaction melt compositions averaged from data collected across the entire IBC half of the diffusion couple

	Initial IBC		MRx#1		MRx#5		MRx#8		MRx#9		MRx#10		MRx#11		MRx#13	
	Avg	σ	Avg	σ	Avg	σ	Avg	σ	Avg	σ	Avg	σ	Avg	σ	Avg	σ
SiO_2	38.03	0.15	34.57	3.67	39.05	0.31	36.31	1.08	38.58	0.58	39.17	0.19	44.65	0.33	35.21	0.34
TiO_2	6.83	0.10	11.84	0.39	5.41	0.22	9.57	0.55	6.83	0.22	5.89	0.13	3.81	0.15	8.72	0.25
Al_2O_3	6.26	0.08	5.59	0.52	5.16	0.28	3.66	1.20	6.21	0.11	5.50	0.18	9.39	0.26	6.36	0.20
Cr_2O_3	0.26	0.01	0.07	0.03	0.25	0.02	0.04	0.02	0.27	0.02	0.25	0.02	0.01	0.02	0.07	0.01
MgO	0.91	0.02	0.48	0.19	7.28	0.65	0.33	0.02	1.22	0.85	6.85	0.32	0.09	0.01	1.99	0.13
CaO	13.91	0.10	10.38	1.96	12.48	0.32	9.59	2.07	14.39	0.43	12.65	0.15	11.47	0.10	11.28	0.45
MnO	1.05	0.02	1.09	0.15	0.94	0.03	1.01	0.04	1.03	0.04	0.92	0.02	1.18	0.03	1.14	0.03
FeO	31.21	0.09	34.07	2.06	28.55	0.35	38.84	3.15	30.97	1.36	28.01	0.19	27.37	0.37	35.55	0.98
NiO	0.00	0.00	0.04	0.06	0.03	0.02	0.01	0.01	0.01	0.01	0.01	0.01	0.01	0.01	0.01	0.01
Na_2O	0.29	0.02	0.49	0.25	0.28	0.03	0.29	0.09	0.30	0.07	0.32	0.05	0.77	0.03	0.26	0.05
Total	98.75	0.23	98.62	0.02	99.43	0.31	99.63	0.82	99.80	0.50	99.57	0.31	98.76	0.24	100.59	0.36
Mg#	4.96	0.12	2.41	0.81	31.20	1.88	1.48	0.20	6.52	4.50	30.34	0.97	0.60	0.04	9.08	0.74

in the low-pressure experiments after quenching (Fig. 5a and b). In contrast, the IBC side of the reaction couple in the high-pressure experiments completely crystallized during quenching, forming dendritic Cpx (Fig. 5c and d). An exception is MRx#9 (0.55 GPa), where the IBC side of the reaction couple is almost entirely glassy with some nano-scale crystals throughout.

The Cpx in the hybridized melt exhibits subhedral, anhedral, or dendritic morphologies. Clinopyroxenes in low-pressure experiments MRx#5 and MRx#10 often exhibit sector or patchy zoning and a bight rim around them (See Supplemental Fig. 3). Clinopyroxene is the only crystallizing phase in MRx#5 and MRx#10. In high-pressure experiment MRx#12, a high-Z phase (presumably an Fe-Ti oxide) is present in the interstitial space between dendritic Cpx; however, crystals were too small to analyze.

MRx#10 exhibits less Cpx crystallization on the IBC side of the reaction interface relative to MRx#5 (Supplemental Figs. 5 and 6). MRx#10 also lacks significant Cpx crystallization throughout the IBC side of the reaction couple (Figs. 5a and b). Clinopyroxene crystals that form on the reaction interface in MRx#5 and MRx#10 are acicular, small, and bright in BSE images (Supplemental Figs. 3 and 4). High-pressure experiment MRx#12 contains abundant Cpx on the reaction interface, and the Cpx is dark in BSE images and pale blue in elemental maps (Figs. 5c and d).

In BSE images, a thin but noticeable diffusive exchange layer is present on the dunite side of the reaction interface

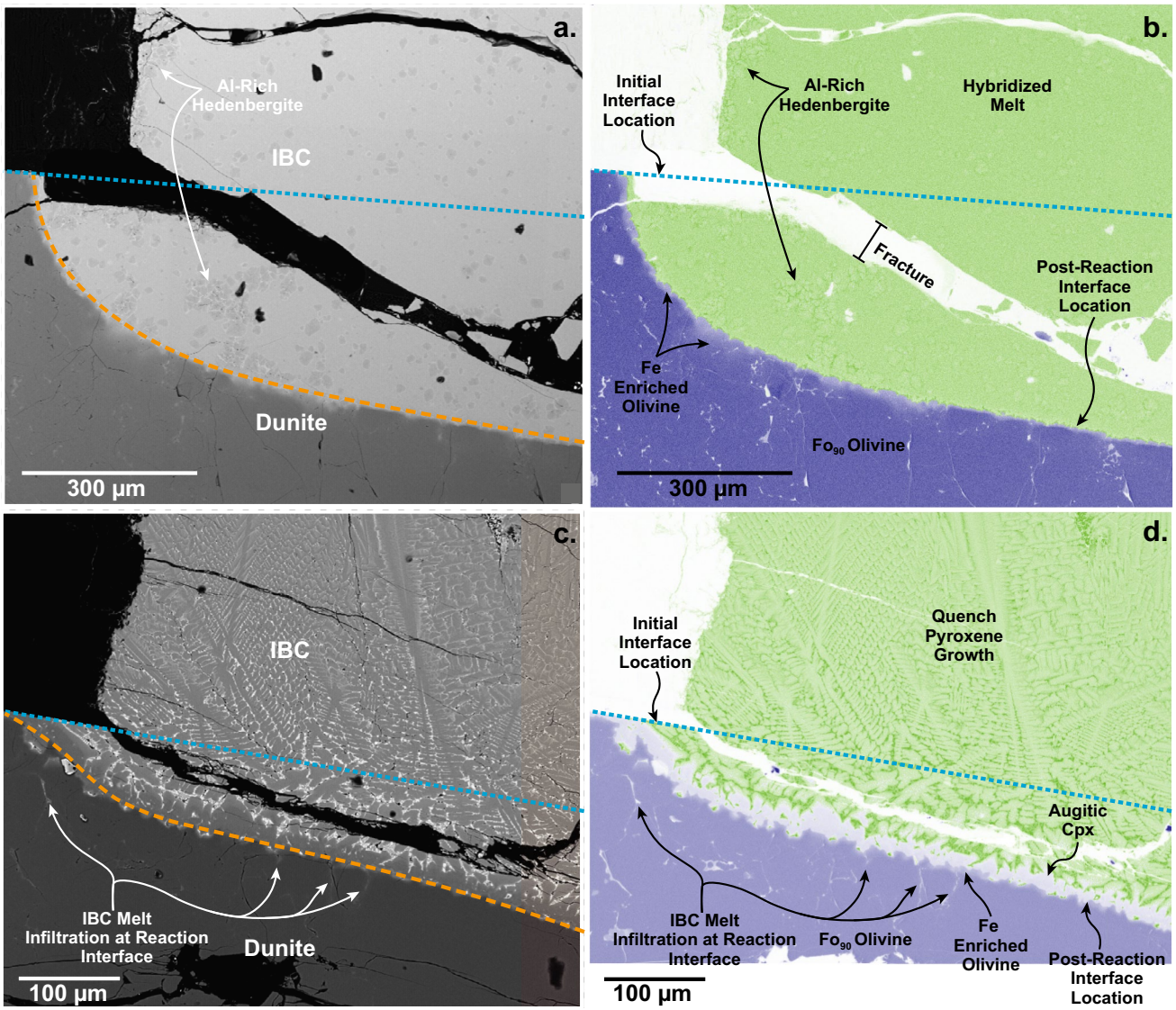

Fig. 5 Representative BSE images and elemental maps highlighting minerals and reaction features in supersolidus experiments. **a** Backscatter electron image of MRx#10 showing the pre-reaction interface, post-reaction interface, and Al-rich hedenbergite. **b** Combined Fe (green) and Mg (blue) false color elemental map of the reaction interface in MRx#10 with phases and reaction features labeled. **c** Backscatter electron image of MRx#12 showing the pre-reaction interface, post-reaction interface, and possible melt propagation into the dunite along grain boundaries. **d** Combined Fe (green) and Mg (blue) false color elemental map of the reaction interface in MRx#12 with phases and reaction features labeled. In all figures the blue dotted line represents the pre-reaction interface position and in figures (**a**) and (**c**) the orange dashed line represents the post-reaction interface position. In both experiments, the IBC-dunite interface has migrated into the dunite side of the reaction couple due to dunite dissolution. In MRx#12 the IBC melt appears to be exploiting grain boundaries to propagate into the dunite resulting in the light gray (**c**) and light blue (**d**) streaks indicated in the dunite

in experiments MRx#10 and MRx#12 with a highly irregular thickness representing concentration gradients in Fe and Mg (Fig. 5b and 5d and Supplemental Fig. 4). MRx#5 and MRx#9 do not have analogous layers on the dunite side of the reaction interface (Supplemental Figs. 3 and 5). The lack of a diffusive exchange layer on the reaction interface may be related to the rate of dunite dissolution relative to solid-state diffusion and is discussed further (in the Dissolution, Diffusion, and Advection section).

Small IBC melt veins were observed along the reaction interface of MRx#5 and MRx#12 (Fig. 5c and d, Supplemental Fig. 3), and some suspected melt infiltration veins were observed near the reaction interface in MRx#9 and MRx#10 (Supplemental Figs. 4 and 5). Veins of melt infiltration are short (< 100 µm), have highly irregular shapes, and are usually next to or in the middle of a thicker portion of the dunite interface layers mentioned above. All group A supersolidus experiments also have thin veins of IBC melt

along the dunite-graphite interface of the assembly (i.e., the assembly walls) that often propagate to the bottom of the dunite half of the reaction couple. The effects of IBC-dunite interface vein formation on the reaction process are discussed further in the subsections on Dunite Dissolution Rates, and Effects of Dunite Dissolution on IBC Liquid and Vein Formation in the discussion.

Group A mineral and melt chemistry

Relative to near solidus experiments, most Cpx crystals in the supersolidus experiments have more enstatite (En) normative and less wollastonite (Wo) normative compositions (Fig. 3b). High-pressure experiment MRx#12 contains Cpx that trend toward ferrosilite (Fs). These pyroxenes are exclusively found far from the reaction interface in the dendritic region of the experiment. Like the near solidus experiments, Cpx crystals that form on the reaction couple interface in MRx#12 have more augitic compositions and plot separately from Cpx that form within the IBC side and further from the boundary (Fig. 5b). Clinopyroxene crystals that form on the reaction couple interface in experiments MRx#5 and MRx#10 were too small to analyze.

Melt hybridization in MRx#5 and MRx#10 is evidenced by the elevated melt Mg#s of ~ 30–31 relative to the Mg# of the pre-reaction IBC material (i.e., ~ 5). Similar melt Mg# elevation is observed near the reaction interface of MRx#9; however, the Mg enrichment is confined to the interface due to the shorter duration of the experiment The Mg#s of hybridized melts in MRx#5, MRx#9, and MRx#10 generally decrease with distance from the reaction interface (see the Dunite Dissolution Rates, and Effects of Dunite Dissolution on IBC Liquid subsection for further discussion).

Group B products and growth textures

In experiment MRx#11, large Cpx (200–1000 μm) are present throughout the IBC side of the reaction couple. All Cpx within this experiment exhibit skeletal and euhedral morphologies and core-to-rim zoning (Supplemental Fig. 5). Euhedral ulvöspinel crystals surround the Cpx and are the only Fe-Ti oxides present in the experiment. MRx#11 contains interstitial melt (i.e., IBC melt that has undergone crystallization and lacks evidence of dunite assimilation) in the form of glass throughout the IBC side of the couple. Glass within this experiment occupies the interstitial space between the large Cpx crystals. Clinopyroxene crystals are abundant at the reaction couple interface and appear to nucleate from the interface, isolating the interface from the evolved melt.

As in the other experiments, there is a thin but obvious diffusive exchange layer on the dunite side of the reaction interface (Supplemental Fig. 5). This diffusive exchange layer is thinner (~ 5 μm) than those observed in 6 h near solidus experiments (~ 10 μm) on the dunite side of the interface (Table 3). IBC melt veins were not observed along the IBC-dunite reaction interface of MRx#11 as in the Group A experiments.

Group B mineral and melt chemistry

Clinopyroxene crystals in MRx#11 have more Wo normative compositions than all other experiments (Fig. 3b). Normal zoning occurs in all Cpx crystals with an average core Mg# of 22.5 ± 4.7 and rim Mg# of 9.2 ± 2.7, consistent with progressive Cpx crystallization in the IBC composition. Clinopyroxenes near the interface plot along a continuum with the core and rim compositions from elsewhere in the experiment but have slightly more En normative compositions closer to the interface (Fig. 3b).

Interstitial melt in MRx#11 lacks the TiO_2 and FeO enrichment observed in the low-degree interstitial melt from MRx#8. This is likely due to the extensive crystallization of ulvöspinel in this experiment, which would keep the TiO_2 and FeO concentrations lower relative to oxide-free experiments. Overall, melt within this experiment exhibits SiO_2, Al_2O_3, Na_2O enrichment and TiO_2, Cr_2O_3, MgO, and FeO depletion relative to the initial IBC composition (Table 4).

Step-cooled experiment

Products and growth textures

Experiment MRx#13 is the only step-cooled experiment (Table 2). Clinopyroxene is the only phase in the IBC side of the couple large enough to analyze. Clinopyroxenes are large (500–1500 μm) and exhibit skeletal and euhedral morphologies like those in MRx#11. Clinopyroxenes within the experiment exhibit pronounced core-to-rim zoning, similar to MRx#11.

High-Z phases (presumably Fe-Ti oxides) are present in the interstitial region between large Cpx. The presence of these phases is most apparent near the IBC-dunite interface where Cpx crystals formed in close proximity to each other, and the hybridized interstitial melt (i.e., IBC melt that has assimilated dunite material and undergone crystallization) seems to have undergone more extensive crystallization.

BSE images show that the experiment resulted in extensive dunite dissolution as the IBC-dunite interface migrated into the dunite side of the reaction couple (Fig. 6a and b). Hybridized interstitial melt is present throughout the IBC side of the experiment. Clinopyroxene crystals are abundant at the reaction couple interface and appear to nucleate from the interface, isolating the interface from the melt. Given the extensive dissolution observed in this experiment, the

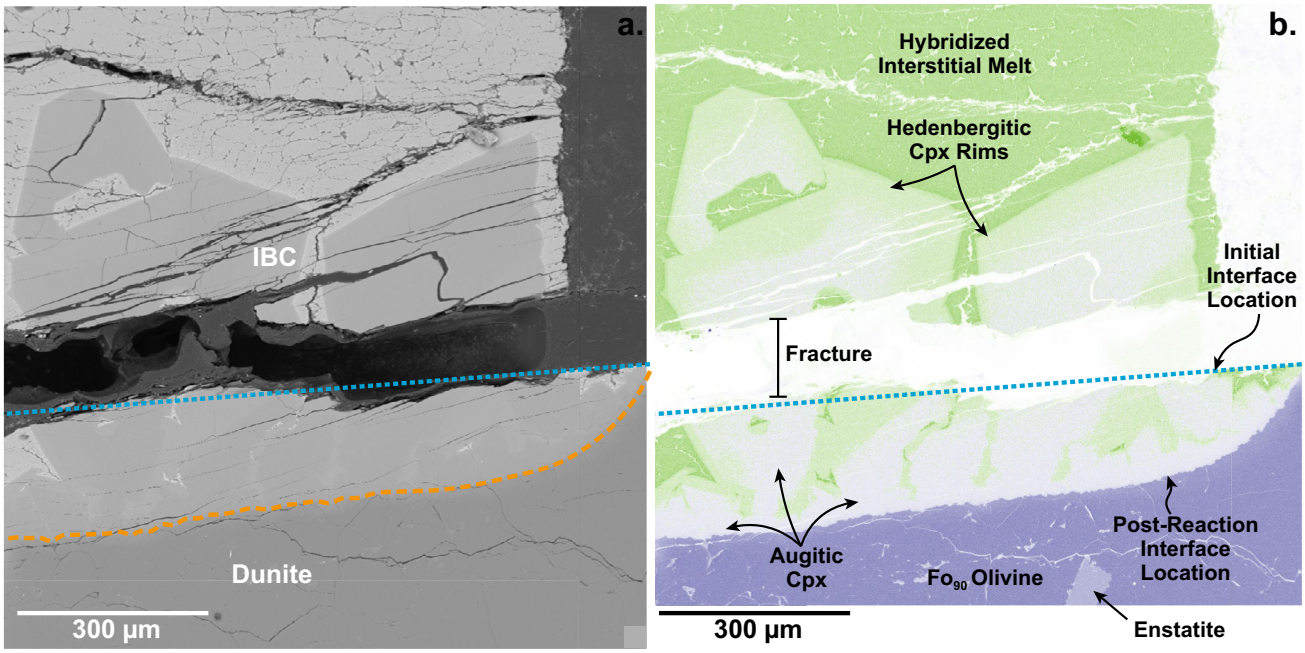

Fig. 6 Representative BSE image and elemental map highlighting minerals and reaction features produced in step-cooled supersolidus experiment MRx#13. **a** Backscatter electron image of the reaction interface showing the pre-reaction interface (blue dotted line) and post-reaction interface (orange dashed line). **b** Combined Fe (green) and Mg (blue) false color elemental map of the reaction interface with the pre-reaction interface, phases, and reaction features labeled. The IBC-dunite interface location has migrated into the dunite side of the reaction couple due to dunite dissolution. A rare enstatite crystal within the dunite side of the reaction couple is visible in the elemental map, this grain is unrelated to melt-rock reaction and originates from incomplete mineral separation in the starting material

Cpx crystals likely formed during the cooling step of the experiment, significantly reducing IBC-dunite interaction.

Mineral and melt chemistry

Clinopyroxene crystals in MRx#13 have unique compositions relative to the other experiments (Fig. 3b). The Cpx are less Fs normative than those observed in the near solidus experiments and MRx#11. The pyroxenes exhibit a continuum of compositions ranging from augitic to hedenbergitic. Clinopyroxene cores have Mg#s of 48.2 ± 5.1, while clinopyroxene rims have Mg#s of 36.3 ± 2.3. Given the morphology and size of the crystals, the core-to-rim zoning perhaps reflects a shift in equilibrium pyroxene compositions as the melt composition evolved due to progressive crystallization.

Hybridized interstitial melt in MRx#13 exhibits TiO_2, MgO, and FeO enrichment and SiO_2, Cr_2O_3, and CaO depletion relative to the initial IBC composition (Table 4). TiO_2 and FeO enrichment and CaO depletion in the melt are consistent with progressive Cpx crystallization and lack of significant Fe-Ti oxide formation. The elevated Mg# reflects extensive dunite dissolution. Crystallization of Cpx probably decreased the total amount of Mg in the melt given the high Mg# of the pyroxene cores and size of the crystals and low Mg# of the hybridized interstitial melt (i.e., 9.08 ± 0.74).

As in other experiments in this study, the boundary between the IBC and dunite sides of the experiment exhibits evidence of solid-state diffusive exchange. The Cpx at the interface in the IBC side of the reaction couple has an elevated Mg# of ~ 71. Olivine in the dunite side of the couple is more Fa normative near the interface (Fo ~ 82).

Discussion

Here we discuss dissolution–precipitation reactions, followed by an analysis of rates of dissolution and diffusive exchange reactions, and veining. Then we discuss phase equilibria in the subsolidus experiments.

Dissolution–precipitation reactions and crystallization in the IBC liquid

Dunite assimilation

Propagation of the reaction interface into the dunite and elevated Mg#s of residual melts in experiments MRx#5, MRx#9, MRx#10, and MRx#13 demonstrate a dissolution reaction produced by Fe-rich melt in contact with an Mg-rich dunite. Dunite dissolution is anticipated according to the low-Mg# (i.e., 25) mare basalt olivine-wollastonite-quartz

ternary diagram from Longhi (1991) (Fig. 7). The initial IBC composition is augite normative and plots above the olivine-augite cotectic (Fig. 7). Since the IBC is at supersolidus temperatures in these experiments, olivine dissolves into the IBC melt as the system reacts and equilibrates. This drives the IBC melt towards a more olivine normative composition, shifting the composition toward the olivine-augite cotectic (Fig. 7). This reaction proceeds following Eq. 1:

$$IBC\ Melt + Olivine \rightarrow Hybridized\ Melt \pm Clinopyroxene, \quad (1)$$

with olivine dissolution progressing until eventual olivine saturation in the hybridized melt. This hybridization process can be modeled by assuming modal mixing between the initial IBC composition and the dunite. Melt compositions from experiments MRx#5 and MRx#10 are consistent with 10–15% dunite assimilation, while melt compositions from MRx#9 are consistent with 0–5% assimilation (Fig. 7). Most melt compositions from experiments MRx#5 (6 h) and MRx#10 (24 h) cluster around the olivine-augite cotectic, and the estimated dissolution rates for these experiments decrease with experiment duration (See Table 3). These observations suggest that dissolution occurs at rates that decrease as the melt composition approaches the olivine-augite cotectic (see the Dunite Dissolution Rates, and Effects of Dunite Dissolution on IBC Liquid subsection below for further discussion).

As dissolution proceeds, the Mg# of the reacting melt increases. It is well known that Mg# variations cause phase boundaries to shift, and stability fields of phases can shrink or expand (e.g., Stolper and Walker 1980; Longhi 1982, 1991; Elthon and Scarfe 1984) (Fig. 7). Previous studies indicate that the olivine-low Ca pyroxene-augite peritectic shifts toward olivine as pressure increases. Similarly, increasing pressure shifts the olivine-augite cotectic downward toward the olivine-silica binary on the phase diagram (Fig. 7).

Crystallization in the IBC melt

Experiment MRx#11 lacks evidence of dunite dissolution and contains a significant melt fraction, in addition to Cpx and ulvöspinel (Supplemental Fig. 6). Melt from this experiment plots between the IBC starting material and the Mg# 25 ternary olivine-pigeonite-augite peritectic, which indicates that the melt is evolving toward the peritectic (Fig. 7). This shift in composition is consistent with the growth of

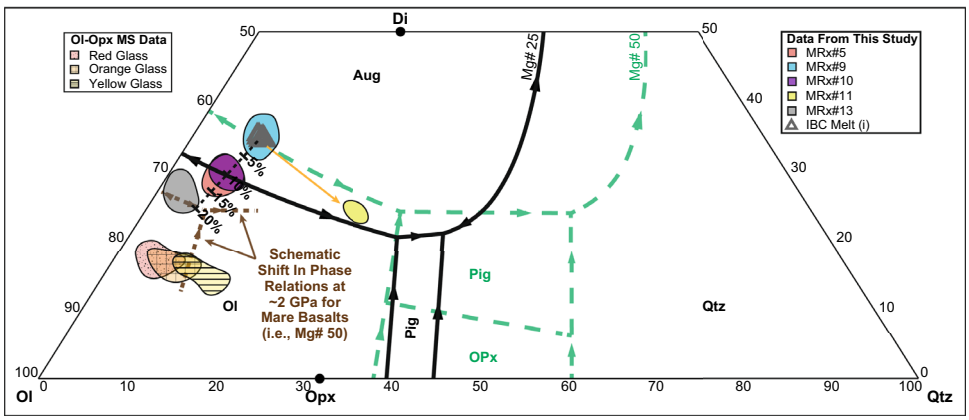

Fig. 7 Experimental glasses plotted in relation to olivine-wollastonite-quartz basalt ternary diagrams from Longhi (1991). The thin black dotted line and shows the trajectory of a simple mixing model for modal dunite addition to the initial IBC liquid between 1 and 20%. Orange solid arrow shows the trajectory for equilibrium crystallization. Solid black phase boundaries and arrows are from basalt projections in a system with an Mg# of 25 and mare basalt relevant alkali components at atmospheric pressure. Dashed green phase boundaries and arrows are from mare basalt relevant projections in a system with an Mg# of 50 at atmospheric pressure. The brown dotted lines are schematic of a pressure related shift in the phase relations for Mg# 50 mare basalts as pressure increases. The schematic boundaries are based on the observations from lunar glass multi-saturation experiments (Krawczynski and Grove 2012; Brown and Grove 2015) and previous studies of basalt phase equilibria (Stolper 1980; Longhi 1982; Elthon and Scarfe 1984). The dotted shaded region represents experimental lunar red glass data for melts at the Ol-Opx saturation point (for pressures of 1.7–2.3 GPa) (Krawczynski and Grove 2012). The cross-hatched shaded region represents experimental lunar orange glass data for melts at the Ol-Opx saturation point (for pressures of 1.9–2.33 GPa) (Krawczynski and Grove 2012). The striped shaded region represents experimental lunar yellow glass data for melts at the Ol-Opx saturation point (for pressures of 1.7–2.3 GPa) (Brown and Grove 2015). Given inferred relationships between mare basalts and lunar picritic glasses and similar Mg#s, these melts define the position of the Ol-Opx cotectic position for Mg# 50 mare basalts (dashed green lines) at pressures of 1.7–2.33 GPa. If the Ol-Opx cotectic shifts towards normative olivine as Mg# increases (as the data imply), the Ol-Pig-Aug peritectic and Ol-Aug cotectic should experience a similar shift in position given the observations from previous studies (Stolper and Walker 1980; Longhi 1982; Elthon and Scarfe 1984). Phases: Olivine (Ol), Orthopyroxene (Opx), Diopside (Di), Augite (Aug), Pigeonite (Pig), Quartz (Qtz)

sizeable euhedral pyroxene and ulvöspinel observed in the experiment.

MRx#13 likely reflects the effects of crystallization after dissolution based on the large size and euhedral morphology of pyroxene crystals from that experiment. Given the extensive pyroxene crystallization observed in MRx#13, the melt is likely at or near the 2 GPa olivine-augite cotectic (Fig. 7) and beginning to evolve to the left (down temperature from a thermal maximum) along the cotectic as crystallization progresses, consistent with predicted evolution trajectories from previous studies. It is difficult to determine how the MRx#13 melt might continue to evolve; however, we speculate that the TiO_2 and FeO enrichment observed in MRx#13 would eventually result in the stabilization of an Fe-Ti oxide phase. Stabilization of the Fe-Ti oxide would enrich melt in Al_2O_3 and SiO_2 and eventually stabilize an aluminosilicate, perhaps garnet at the conditions of the experimental run, forming a hybridized lunar eclogite (See the Phase Equilibria section below for further discussion). Further experimental work is required to evaluate this hypothesis.

Dissolution, diffusion, and advection

Solid-state diffusion

Near solidus experiments MRx#1, MRx#3, and MRx#8 exhibit compositional variations across the IBC (Cpx) and dunite (olivine) sides of the reaction couple interface consistent with diffusive exchange, with Mg-enriched pyroxene on the IBC side and Fe-enriched olivine on the dunite side. Supersolidus experiments MRx#10, MRx#11, and MRx#12 also exhibit compositional variations on the dunite side of the reaction interface, with Fe-enriched olivine at the interface boundary. However, given the complexity of dissolution shifting the IBC-dunite interface location, crystallization at the interface changing the melt composition, and the multi-step nature of some experiments, no attempt was made to model diffusive interaction for experiments MRx#10, MRx#11, MRx#12, and MRx#13. Diffusive exchange models are applied to near solidus experiments MRx#1 and MRx#8.

In MRx#1 and MRx#8, the IBC side of the couple exhibits a downward shift in molar $Fe/(Fe+Mg)\times100$, while the dunite side of the couple exhibits an upward shift (Fig. 8). Both experiments exhibit similar interface conditions with compositional variations trending toward $Fe/(Fe+Mg)\times100$ values between 40 and 50. Compositional variations in 24 h experiment MRx#8 (1150 °C) are approximately twice the width of the variations in 6 h experiment MRx#1 (1200 °C), 1150 °C vs 1200 °C respectively. These compositional variations were modeled using an analytical solution to the one-dimensional diffusion equation assuming exchange between two semi-infinite media with differing diffusivities and a partitioning relationship across the interface (Zhang 2009) (See Online Supplement for details). From MRx#1, we recover an effective diffusivity of $5.34\times10^{-16}\pm1.46\times10^{-16}$ m^2/s in the dunite and $3.34\times10^{-16}\pm9.48\times10^{-17}$ m^2/s in the IBC (Fig. 8a). The model for MRx#8 recovers an effective diffusivity of $8.96\times10^{-16}\pm1.36\times10^{-16}$ m^2/s in the dunite and $8.15\times10^{-16}\pm1.57\times10^{-16}$ m^2/s in the IBC (Fig. 8b).

The Fe–Mg diffusion rates for IBC determined by this study are three to four orders of magnitude faster than anticipated at 1200 °C to 1100 °C for Cpx according to volume diffusion studies (Brady and McCallister 1983; Fujino 1990; Azough and Freer 2000; Zhang et al. 2010a; Müller et al. 2013). Fe–Mg diffusion in garnet is faster than Cpx; however, the IBC exchange rates from this study are still one to two orders of magnitude faster at the relevant temperatures (Loomis et al. 1985; Chakraborty and Ganguly 1992; Chakraborty and Rubie 1996; Ganguly et al. 1998; Perchuk et al. 2009; Borinski et al. 2012; Li et al. 2018). It is possible that the Fe-rich compositions of minerals within the IBC material accelerate diffusive exchange relative to the existing data from more magnesian experiments, as diffusion through Fe-rich endmembers is often faster than diffusion through Mg-rich endmembers (e.g., Buening and Buseck 1973; Nakamura and Schmalzried 1984; Chakraborty 1997; Dohmen and Chakraborty 2007). The presence of trace amounts of interstitial melt and polycrystalline nature of the IBC may also affect the diffusion rates on the IBC side of the reaction couple. Grain boundary diffusion is expected to be three orders of magnitude faster than volume diffusion (Farver et al. 1994).

Dunite Fe–Mg diffusion rates determined for MRx#1 and MRx#8 fall within the range of diffusivities determined from previous experimental studies at temperatures between 1200 °C and 1100 °C (i.e., 10^{-14} to 10^{-17} m^2/s) (Jurewicz and Watson 1988; Chakraborty et al. 1994; Chakraborty 1997; Petry et al. 2004; Dimanov and Wiedenbeck 2006; Dohmen and Chakraborty 2007). Faster diffusion rates in MRx#8 appear inconsistent with the 50 °C temperature difference between MRx#1 (1200 °C) and MRx#8 (1150 °C). According to previous olivine diffusion studies, the diffusion rates should be about half an order of magnitude faster in MRx#1 if temperature is the only factor affecting the rate. We interpret the results as demonstrating the dependence of diffusion rate on olivine Fe/Mg content, with fayalitic olivine exchanging Fe for Mg about three orders of magnitude faster than forsterite (Chakraborty 1997; Dohmen and Chakraborty 2007). The higher iron content in the diffusive boundary layer increases the exchange rate such that longer experiments have faster effective diffusion rates.

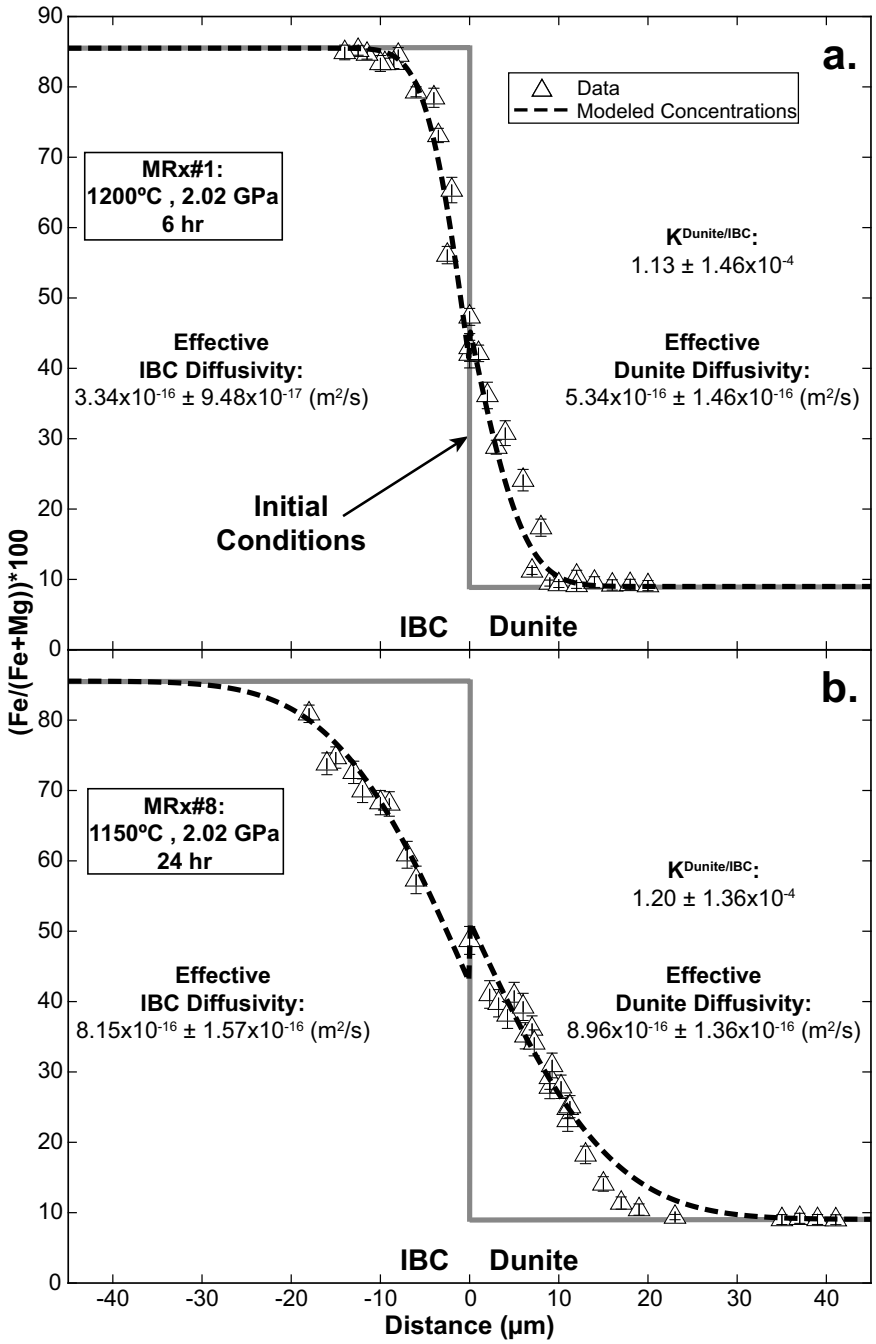

Fig. 8 Fe–Mg exchange profiles across the IBC-dunite interface from near solidus experiments. **a** Fe–Mg exchange profile from experiment MRx#1. **b** Fe–Mg exchange profile from experiment MRx#8. Gray solid lines show the initial conditions prior to reaction. Dashed lines are modeled concentration profiles for the reaction couple

Dunite dissolution rates, and effects of dunite dissolution on IBC liquid

Constant temperature (1200 °C), low-pressure (0.55 GPa) experiments run for 20 min (MRx#9), 6 h (MRx#5), and 24 h (MRx#10) enable us to investigate the dunite dissolution rate as a function of time and compare compositional variations in the coexisting IBC melt affected by dissolution. In the IBC melt, MRx#5 and MRx#10 exhibit unusual MgO, Al_2O_3, and TiO_2 concentration variations that peak ~ 100–200 µm away from the reaction interface, consistent with uphill diffusion. The concentrations of these elements then decline as approximately linear trends away from the peaks toward the end of the IBC half of the reaction couple (Fig. 9a, d, e). CaO concentrations exhibit similar trends with the lowest concentrations ~ 100–200 µm away from the reaction interface and concentrations that ascend linearly toward the end of the IBC half of the reaction couple (Fig. 9f). These compositional variations may be produced by multi-component diffusion effects, where coupled concentration variations affect diffusion rates and elemental variations (e.g., Zhang 1993; Morgan et al. 2006; Van Der

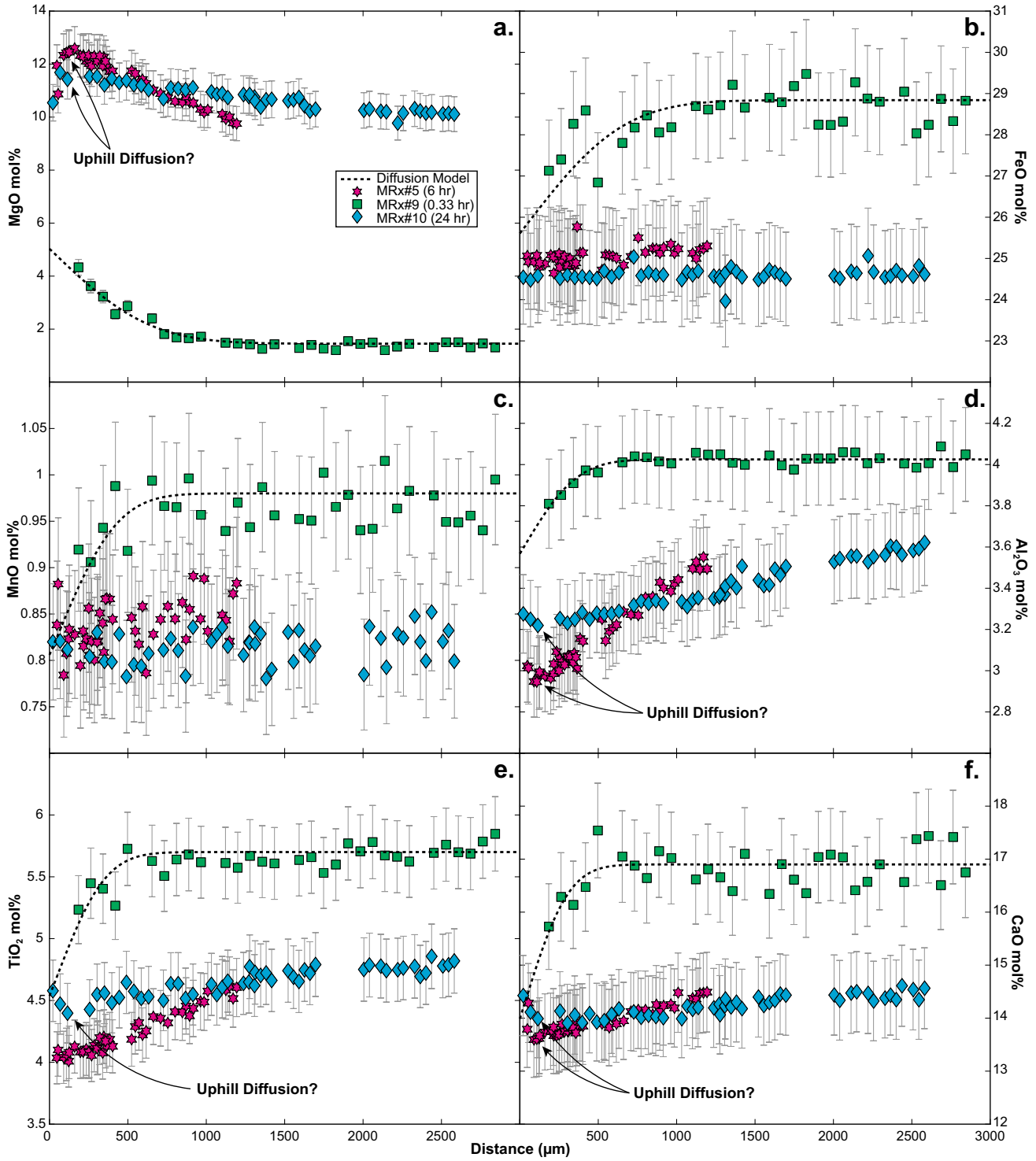

Fig. 9 Elemental concentration profiles in the IBC melt from the reaction interface (i.e., 0 μm) to the top of the experiment (or top of the glass-dominated region of the experiment). Modeled diffusion profiles for MRx#9 with respect to **a** MgO, **b** FeO, **c** MnO, **d** Al_2O_3, **e** TiO_2, and **f** CaO mol% are represented by the dashed line. In contrast to experiment MRx#9, MRx#5 and MRx#10 exhibit **b** MgO, **d** Al_2O_3, **e** TiO_2, and **f** CaO variations consistent with uphill diffusion at the melt-rock interface, these experiments were run for hours whereas MRx#9 was run for 20 min (see legend). Distances for MRx#5, MRx#9, and MRx#10 data were determined by measuring the distance between the reaction interface and first point of the chemical transect. Sizable fractures were present near the interface of MRx#9 and ~ 1800 μm from the interface in MRx#10 resulting in data gaps. Parameters recovered from MRx#9 diffusion model fits can be found in Table 5. All experiments in this figure were run at 0.55 GPa and 1200 °C

Table 5 Effective binary diffusion coefficients (EBDC) of MgO, FeO, MnO, Al_2O_3, TiO_2, and CaO for dunite dissolution in IBC melt at 1200 °C, 0.55 GPa

	MgO		FeO		MnO		Al_2O_3		TiO_2		CaO	
	val	1σ	val	1σ	val	1σ	val	1σ	val	1σ	val	1σ
EBDC (m^2/s)	9.84E-11	1.36E-11	9.67E-11	5.28E-11	3.83E-11	3.57E-11	3.00E-11	1.29E-11	2.56E-11	1.86E-11	2.02E-11	2.49E-11
C_0 (mol%)	5.03	0.30	25.61	0.98	0.81	0.12	3.57	0.17	4.54	0.74	13.99	3.66
a	0.035	0.003	0.081	0.091	0.120	0.081	0.067	0.004	0.125	0.050	0.105	0.079
Dissolution rate (g m^{-2} $s^{-1/2}$)	1.15	0.13	2.62	3.03	2.43	2.00	1.21	0.27	2.08	1.12	1.55	1.51
Average dissolution rate (g m^{-2} $s^{-1/2}$)	1.84	0.68										

For dissolution rate calculations the estimated melt ρ = 3.286 (g/cm^3). This was determined using the method of Bottinga and Weill (1970). Volume, thermal expansion, and compressibility data from Lange and Carmichael (1987) and Kress and Carmichael (1991) were used for the calcaulation

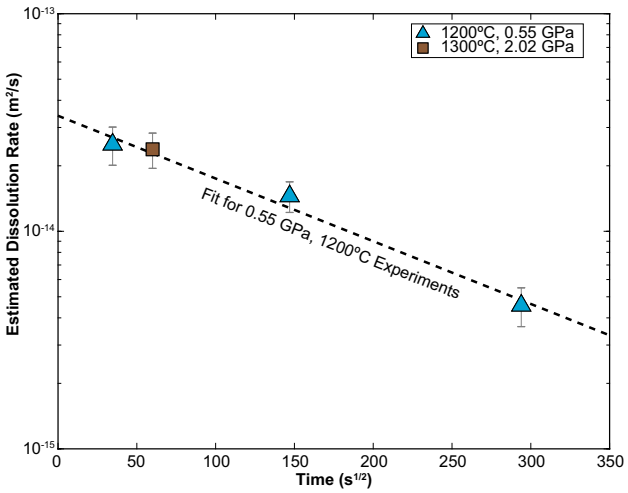

Fig. 10 Dunite dissolution rates plotted against the square root of time. Experiment MRx#12 was used to calculate the dunite dissolution rate at 1300 °C and 2.02 GPa. Experiments MRx#5, MRx#9, and MRx#10 were used to calculate rates at 1200 °C and 0.55 GPa

Laan et al. 1994; Zhang et al. 2010b; Liang 2010). Modeling multi-component diffusion is beyond the scope of this study.

Dissolution of olivine in the dunite occurs quickly causing the MgO mol% in the IBC melt near the interface to increase to 5.03 ± 0.30 in the 0.33 h experiment (Fig. 9a, Table 5). Chemical profiles from MRx#9 were modeled using an analytical solution for one-dimensional diffusion-controlled dissolution into a semi-infinite melt reservoir (e.g., Zhang et al. 1989; Van Orman and Grove 2000) (Fig. 9) (See Online Supplement for calculation details). Effective binary diffusion coefficients for MgO, FeO, MnO, Al_2O_3, TiO_2, and CaO in the IBC melt were inverted from the compositional observations by a nonlinear least squares regression. The inverted EBDCs of MgO, FeO, MnO, Al_2O_3, TiO_2, and CaO in the IBC melt at 1200 °C and 0.55 GPa, all fall between 10^{-10} and 10^{-11} m^2/s, respectively based on data from MRx#9 (Table 5). Van Orman and Grove (2000) calculate similar EBDCs of $1.92 \times 10^{-10} \pm 7.7 \times 10^{-11}$ m^2/s for MgO, $2.5 \times 10^{-11} \pm 6.3 \times 10^{-12}$ m^2/s for Al_2O_3, and $2.87 \times 10^{-11} \pm 1.0 \times 10^{-11}$ m^2/s for TiO_2 at a higher temperature of 1350 °C and 1.3 GPa for an analogous melt composition. Using the calculated EBDCs and the relationship between EBDC, mineral density, and the dimensionless parameter *a* described in Zhang et al. (1989), we estimate a mean dissolution rate of 2.07 ± 0.87 gm^{-2} $s^{-1/2}$ for dunite in MRx#9, within uncertainty of measured mean dissolution rate of 2.18 ± 0.59 gm^{-2} $s^{-1/2}$ for diopside determined by Van Orman and Grove (2000).

Observing the change between the melt-rock interface position before and after the reaction experiments, we estimated the rate of interface retreat with respect experiment duration (Fig. 10) (Table 3). These data indicate that the

rate of interface retreat decreases as experimental duration increases (i.e., dunite dissolution slows over longer periods of time). We speculate that the decreasing dissolution rate is related to the degree of undersaturation of olivine in the IBC melt as it approaches the augite-olivine cotectic (Eq. 1). A similar change in dissolution rate was previously observed in low-temperature experimental studies, e.g., labradorite and gibbsite dissolution experiments, where the rate of dissolution decreased by a factor of ~ 4.5 as the saturation of the mineral in the solution increased (Nagy and Lasaga 1992; Taylor et al. 2000). The changing dissolution rate may also explain the lack of concentration variations in the dunite along the reaction interface of experiments MRx#9 and MRx#5. The rate of dunite dissolution in these experiments may exceed the rate of diffusive exchange within the dunite, so a diffusive exchange layer never forms in the dunite. Concentration variations along the dunite interface of MRx#10 formed because the melt became closer to olivine saturation, at which point the rate of diffusion in olivine exceeded the rate of dunite dissolution.

Vein formation

The formation of veins along the IBC-dunite reaction interface in supersolidus experiments highlights the possible importance of advective infiltration mechanisms on lunar mantle hybridization. Melt infiltration features are often observed at the reaction interface in experimental studies exploring melt-rock reaction (Morgan and Liang 2003, 2005; Beck et al. 2006; Van Den Bleeken et al. 2010; Pec et al. 2020). These features are similar in scale to the veins in this study but are typically associated with pyroxene dissolution. Veins in MRx#12 appear to follow grain boundaries toward triple junctions (Supplemental Fig. 7). We speculate that olivine grain boundaries provide a permeable path for IBC melt to infiltrate the dunite and enhance the dissolution rate. This infiltration and dissolution process explains the jagged texture along the dunite interface. As grain boundaries dissolve, smaller residual cores are left behind.

Phase equilibria

Supersolidus and near solidus experiments MRx#1, MRx#3, MRx#8, and MRx#11 suggest that both Fe-Ti oxide and silicate mineral phase transitions occur at temperatures between 1100ºC and 1150ºC and pressures above 2.1 GPa (Fig. 11). Below, we compare the observations from this study and previous experimental studies and discuss their implications for IBC phase equilibria.

Fe-Ti oxides

Results from this study and previous work (Van Orman and Grove 2000; Thacker et al. 2009; Mallik et al. 2019) suggest ulvöspinel stability is temperature dependent, with ulvöspinel absent in high-temperature experiments. Ulvöspinel is absent at 1050 °C and 0.0001 GPa (Van Orman and Grove 2000) and in the 2 GPa experiments from Mallik et al. (2019) and the current study conducted above 1100 °C. Existing experimental data show no clear preference for either oxide between 1050 °C and 1100 °C; however, this may be related to compositional variations in the starting material (i.e., the higher FeO and lower TiO_2 composition in this study (Table 1.)) or the fO_2 conditions of the experiments (Anovitz et al. 1985; Shepherd et al. 2022). Given the absence of ulvöspinel in higher temperature experiments, we infer that ilmenite is the only oxide present at temperatures above ~ 1110 °C at atmospheric pressure and ~ 1140 °C at 2 GPa. At P–T conditions beneath the ilmenite-only stability field (i.e., < 1110 °C at atmospheric pressure and < 1140 °C at 2 GPa), we infer that ilmenite and ulvöspinel can coexist (Fig. 11).

Armalcolite is a common Fe-Ti oxide observed in lunar rocks (Haggerty 1973), but was not observed in the experiments from this study. If we consider the results of MgO-FeO-Fe_2O_3-TiO_2 and FeO-Fe_2O_3-TiO_2 system experiments (Haggerty and Lindsley 1970; Friel et al. 1977), thermodynamic models (Xirouchakis et al. 2002; Xirouchakis 2007), and peridotitic experiments of Thacker et al. (2009), armalcolite would be expected in MRx#11; however, its absence in this experiment and similar experiments reported by Van Orman and Grove (2000) indicate that armalcolite is not stable within the IBC-like systems at near-solidus conditions. With a lower metal:anion proportion than ilmenite, the stability of armalcolite may be fO_2-dependent. Experiments of Shepherd et al. (2022), stabilized armalcolite in Ti–rich ferrobasaltic at fO_2 > FMQ, but not at lower lunar relevant, fO_2 conditions.

Garnet

Garnet in the IBC side of the reaction couple at ~ 2 GPa is novel but may be anticipated given the stability of garnet in terrestrial mafic granulites and eclogites at pressures of ~ 1.5–2.0 GPa (Cohen et al. 1967; Ito and Kennedy 1971; Springer and Seck 1997), which have bulk compositions comparable to the IBC material explored here. Mallik et al. (2019) show that garnet can be stable in an IBC cumulate and synthetic hybridized mantle sources; however, this was at pressures of ~ 4.5 GPa (i.e., analogous to the lunar core-mantle boundary). Multi-saturation experiments of red and green picritic glasses and Apollo 17 mare basalts indicate that garnet may be stable in the lunar mantle at pressures

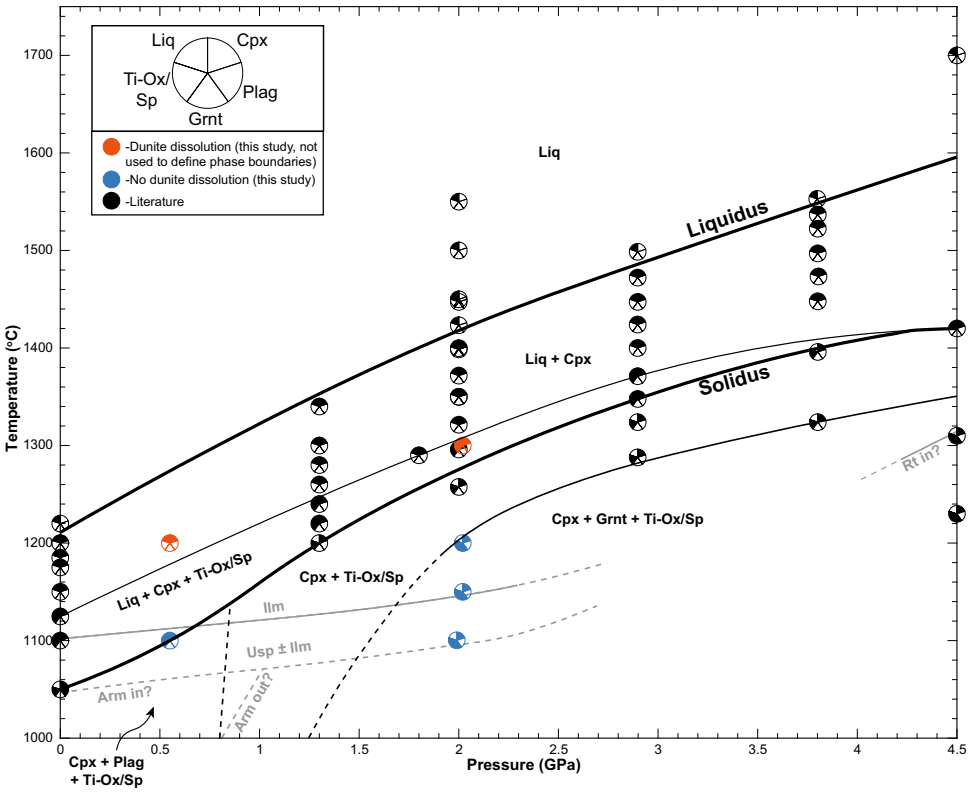

Fig. 11 Ilmenite bearing cumulate phase diagram based on the observations from this work and previous experimental studies testing IBC and Ti–rich lunar relevant compositions (Haggerty and Lindsley 1970; Friel et al. 1977; Wyatt 1977; Van Orman and Grove 2000; Xirouchakis et al. 2002; Mallik et al. 2019). New experimental data from this study are blue and orange points representing experiments that did not and did exhibit dunite dissolution, respectively. Literature data are shown in black (Wyatt 1977; Van Orman and Grove 2000; Mallik et al. 2019). Experiments which resulted in dunite dissolution (orange) were not used to determine phase boundaries for the IBC. Black lines represent silicate assemblage boundaries ± oxides while gray lines indicate Fe-Ti oxide boundaries. Solid lines represent boundaries estimated using data from experiments conducted on IBC-related compositions. Solidus and liquidus are shown as thicker lines. Dashed lines represent phase boundaries inferred from non-IBC specific studies or trajectories of solid lines. Armalcolite phase boundaries in the lower left corner of the diagram are based on the results of Haggerty and Lindsley (1970), Friel et al. (1977), Xirouchakis et al. (2002), and Thacker et al. (2009). Dashed plagioclase stability boundary in the lower left corner of the diagram is an extrapolation based on the plagioclase stability boundary in the modeled TWM phase diagram from Johnson et al. (2021). Phases: Liquid (Liq), Clinopyroxene (Cpx), Plagioclase (Plag), Garnet (Grnt), Fe-Ti Oxide or Spinel (Ti-Ox/Sp), Ilmenite (Ilm), Ulvöspinel (Usp), Armalcolite (Arm), Rutile (Rt)

slightly above 2 GPa (Longhi et al. 1974; Elkins-Tanton et al. 2003; Krawczynski and Grove 2012; Barr and Grove 2013). THERMOCALC models for LPUM and TWM compositions presented in Johnson et al. (2021) suggest that the garnet stability field may extend closer to ~ 1.25 GPa at 1000 °C.

Garnets produced in our experiments are almandine normative relative to terrestrial garnets and garnets from previous experimental lunar studies (Fig. 4). This is a consequence of the low Mg# of starting the IBC composition (Table 1). While the lower Mg# decreases the solidus temperature of the IBC composition in this study relative to previous work, the new results and literature suggest it has a negligible effect on the pressure at which garnet becomes stable (Longhi et al. 1974; Elkins-Tanton et al. 2003; Krawczynski and Grove 2012; Barr and Grove 2013). Considering these results, we infer garnet will be stable in overturned IBC in the lunar interior at pressures around 2 GPa; however, garnet stability may extend toward lower P–T conditions (Fig. 11). This is significant as garnet is not predicted to be a product of lunar magma ocean solidification for bulk Moon compositions with Al_2O_3 contents in agreement with crustal thickness constraints (i.e., LPUM; Elardo et al. 2011; Taylor and Wieczorek 2014; Charlier et al. 2018). Formation of metamorphic garnet in downwelling IBC during cumulate mantle overturn represents a plausible mechanism for delivering geochemical signatures of garnet to hybridized lunar basalt source regions. This is discussed further in Metamorphic Reactions section below.

Implications for the Lunar mantle

Density-driven overturn of late crystallizing IBC would juxtapose the IBC material and mafic early crystallizing LMO cumulates, promoting metamorphic reactions, melting, mineral dissolution, thermal diffusion, and elemental diffusion that led to hybridization of lunar mantle basalt sources. Mechanical mixing due to cumulate overturn or subsequent convective stirring would further mix lunar basalt sources. In this section, we discuss the first-order implications of melt-rock reaction experiments from this study concerning chemical implications of lunar cumulate overturn.

Metamorphic reactions

Our experiments demonstrate that metamorphic reactions would change the mineralogy of downwelling cumulates during an overturn event. Considering the Fe-Ti oxide phase stability boundaries (Fig. 11), ilmenite is likely the primary oxide phase within the cumulate during cumulate overturn (assuming the thermal profiles from previous studies are reasonable; Elkins-Tanton et al. 2011; Lin et al. 2016; Zhang et al. 2017) (See Supplemental Fig. 8). Ulvöspinel may be present in the IBC at lower pressures (i.e., before overturn or early in the overturn process); however, the temperature increase which the IBC would experience during overturn makes it unlikely to be stable beyond ~ 200 km depth in the lunar interior (i.e., 1 GPa). The near-solidus experiments demonstrate the stability of garnet in downwelling IBC under lunar conditions, in contrast to expectations from lunar magma ocean solidification experiments, which found it was only stabilized in the lunar mantle for unrealistically aluminous bulk Moon compositions (Elardo et al. 2011; Jing et al. 2022; Kraettli et al. 2022).

Garnet stability is dependent on the Al_2O_3 abundance of the system and should thereby be affected by the efficiency of plagioclase floatation during magma ocean solidification (e.g., Dygert et al. 2017; Charlier et al. 2018), as more efficient flotation would produce a less aluminous downwelling IBC cumulates. Interestingly, the garnet stability field for the IBC in this study overlaps with the Ol-Opx multi-saturation pressures for lunar picritic glasses (Supplemental Fig. 8; Elkins-Tanton et al. 2003; Draper et al. 2006; Krawczynski and Grove 2012; Barr and Grove 2013; Brown and Grove 2015). As stated in the introduction, multiple studies have suggested that the lunar mare basalts and picritic glasses are the result of mixing between initially deep Mg-rich sources and initially shallow Ti–rich sources in the lunar cumulate pile (Hess and Parmentier 1995; Van Orman and Grove 2000; Elkins-Tanton et al. 2002; Longhi 2006; Singletary and Grove 2008; Mallik et al. 2019). A downwelling Al and Ti–rich garnet-bearing IBC could mechanically or reactively (by assimilation or diffusive exchange) mix with underlying mafic cumulates and result in the formation of a hybridized source capable of generating mare basalts.

Partial melting of downwelling, garnet-bearing IBC would hybridize the surrounding mantle with melts that have a residual garnet trace element signature, analogous to terrestrial granulite facies melting (Cohen et al. 1967; Springer and Seck 1997). The results of this study provide strong support for the melting of a metamorphosed IBC, a hybridization mechanism previously suggested by Schmidt and Kraettlli (2022). Beard et al. (1998) argue that the extreme Lu/Hf fractionation observed in mare basalts can be best explained by the melting of a garnet-bearing source followed by continued melting in the spinel stability field. The fractionated REE-patterns with $(Sm/Yb)_N$ up to 3.5 in some of some lunar glasses have been argued to originate from a garnet-bearing source (Neal 2001). Stabilization of garnet in downwelling IBC provides a mechanism for forming it in the sources of these basalts.

Formation of hybridized mantle sources: mixing, dissolution, and diffusion

Hybridization of the lunar mantle during cumulate overturn likely happens by multiple processes. The downwelling IBC would produce melts as the IBC descended and sank through the hot underlying mantle, increasing in temperature (See Supplemental Fig. 8). Results from this study show that IBC melts would be significantly undersaturated with respect to forsteritic olivine, and interactions with the underlying Mg-rich cumulates would result in rapid dissolution. As dissolution progresses, the degree of olivine undersaturation in the IBC melt decreases, and a Mg-enriched hybridized melt forms (Eq. 1).

If we assume that olivine is present in the picritic glass source (Longhi et al. 1974; Walker et al. 1974; Delano 1980 1986; Elkins-Tanton et al. 2003, Grove and Krawczynski 2009) and the olivine-liquid $K_{D(Fe/Mg)} \approx 0.34–0.23$ (depending on the TiO_2 concentration within the melt) (Roeder and Emslie 1970; Longhi et al. 1978; Delano 1980; Xirouchakis et al. 2001; Canil and Bellis 2008; Krawczynski and Grove 2012), the picritic glass sources should have Mg# ~ 68–87. Thus, if mantle hybridization during overturn formed the sources of lunar picritic glasses, the hybridized source must reach compositions containing ≥ 47% normative dunite (Fig. 12). The range of compositions in IBC melts for dissolution experiments MRx#5 and MRx#10 indicate that the IBC material incorporated ~ 10–15% dunite (Figs. 8 and 12). This suggests

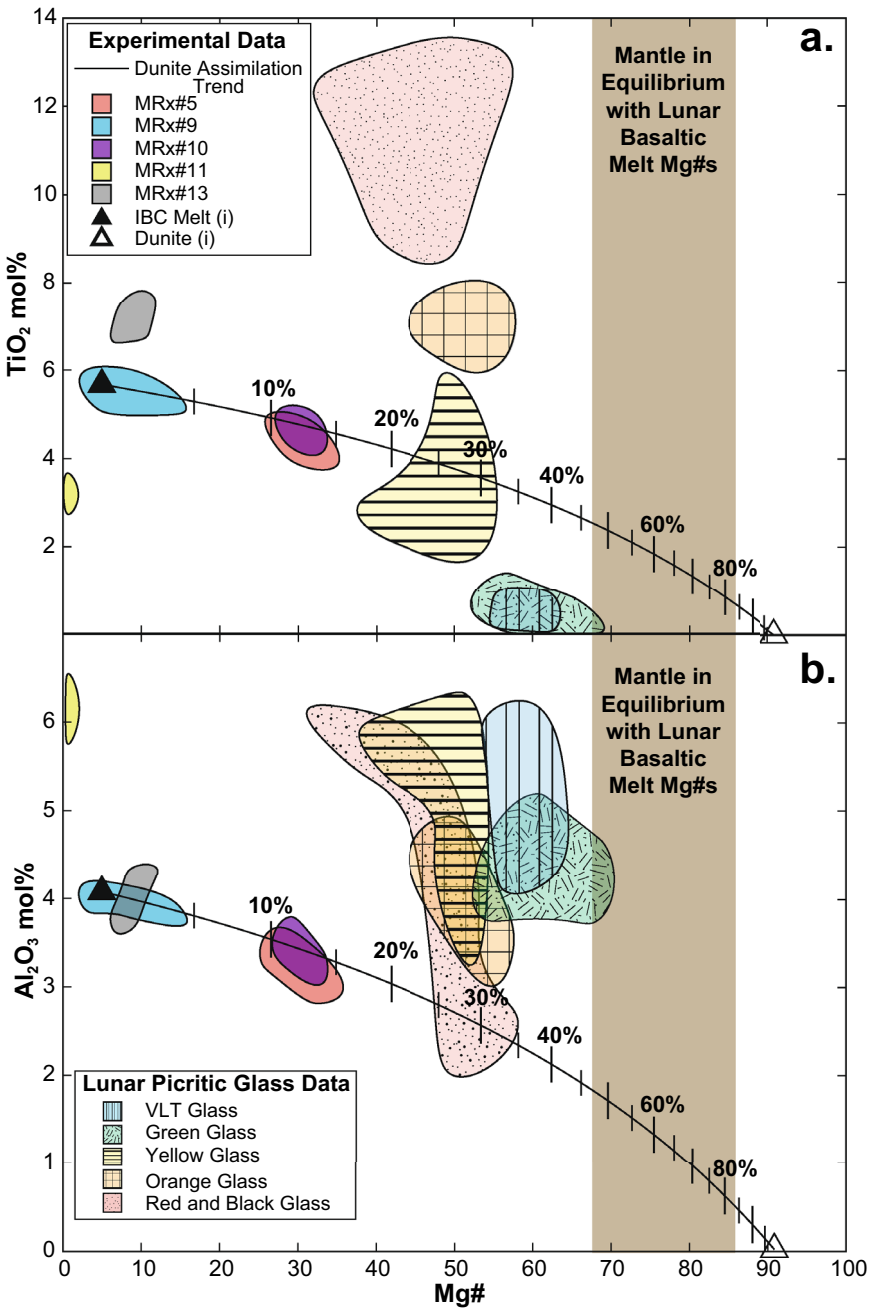

Fig. 12 Comparison of glasses from melt-rock reaction experiments to lunar picritic glasses (TiO_2 mol% vs Mg# (a.) and Al_2O_3 mol% vs Mg#(b.)). Initial IBC melt composition (filled triangle) and initial dunite composition (open triangle) are located at the ends of a calculated dunite assimilation line (black). Percentages represent the amount of dunite assimilated by the IBC melt relative to the initial mass of the IBC melt. Shaded region each plot represents the range of lunar basalt mantle source Mg#s assuming a $K_{D_{Ol-Liq}}^{Fe-Mg} \approx 0.34$–$0.23$, depending on the TiO_2 concentration (Roeder and Emslie 1970; Longhi et al. 1978; Delano 1980; Xirouchakis et al. 2001; Canil and Bellis 2008; Krawczynski and Grove 2012). Lunar data were compiled from Hughes et al. (1990), Shearer et al. (1991), and Shearer and Papike (1993)

that 10–15% of dissolution-driven hybridization could occur relatively quickly (i.e., hours to days); however, observations from this study indicate that the hybridization rate may slow significantly after this initial stage. As the degree of olivine undersaturation decreases, the rate of dunite dissolution decreases (Figs. 7 and 10) (e.g., Watson et al. 1982; Zhang et al. 1989; Watson and Baker 1991; Nagy and Lasaga 1992; Kerr 1995; Liang 2000, 2010; Taylor et al. 2000; Zhang and Xu 2003). Dunite dissolution will only be an effective hybridization mechanism if the composition of melt near the interface remains olivine undersaturated. Replenishment of IBC melt to the dunite-melt interface would be achieved by porous flow or solid-state advection away from the interface.

Comparing the estimated rates of dissolution (Fig. 10) and diffusion (Fig. 9) from this study (see the Dissolution, Diffusion, and Advection section of the discussion), at the experimental conditions, diffusive exchange is at least two orders of magnitude slower than dissolution. Given estimated age of the Moon (i.e., ~ 4.45 Ga: Borg and Carlson 2023 and references therein), bounds on timescales of LMO solidification (i.e., 1000 yr–400 myr after accretion: Solomon and Longhi 1977; Elkins-Tanton et al. 2011; Maurice et al. 2020, 2024), bounds on

timescales for cumulate overturn events (i.e., 10–600 myr after IBC formation: Zhang et al. 2017; Li et al. 2019; Maurice et al. 2024), and age range of High-Ti mare basalts (i.e., ~ 3.89–3.61 Ga; Unruh et al. 1984; Paces et al. 1991; Beard et al. 1998; Sprung et al. 2013; Borg et al. 2019), the formation of lunar basalt sources by mantle hybridization must have been achieved within tens to hundreds of millions of years. Over these timescales, diffusive exchange alone could be limited to length scales of cm to meters around the IBC (Supplemental Fig. 9a). The polycrystalline nature of mantle peridotites means that grain boundary diffusion may increase diffusion rates. Enhanced effective diffusivity owing to multidomain or other diffusion effects could extend the maximum diffusion distance to a few tens of meters over 100 Myr, assuming diffusivities three orders of magnitude faster than the experimental constraints (Supplemental Fig. 9b). The efficiency of diffusive hybridization may depend on the scale of the downwelling IBC plumes. If many plumes form over short wavelengths on the order of kms as predicted by Li et al. (2019), diffusion may be a viable hybridization mechanism over geologically relevant timescales. If the scale of the downwelling IBC instabilities is larger, other mechanisms must be invoked.

Vein formation like that observed along the IBC-dunite interface in supersolidus experiments could enhance the rate of lunar mantle hybridization process. The veins appear to exploit regions of permeability in the mantle material (i.e., the grain boundary between mineral grains). Advection (density-driven sinking) of IBC material through the mantle on scales predicted by previous studies (i.e., Zhang et al. 2017, 2022; Li et al. 2019) could result in strain localization around the downwelling IBC. Strain localization would produce dynamic recrystallization, decreasing grain size in the surrounding mantle material, and producing a greater density of grain boundaries for IBC melt veins to exploit (Van der Wal et al. 1993; Dannberg et al. 2017 and references therein).

If diffusive and dissolutive hybridization mechanisms are insufficiently rapid, mechanical mixing of downwelling IBC and ambient peridotite must be invoked. Poor physical and chemical constraints on material properties related to overturn-driven hybridization make these processes difficult to evaluate. Future studies on (1) the evolving mineralogy of the IBC during P–T changes, (2) melt extraction efficiency from the IBC, (3) the density of the IBC melts, (4) rheological properties of the IBC melt, IBC solid, and surrounding mantle, and strain partitioning among them, (5) lunar mantle and IBC deformation rates, (6) thermal states of the IBC and surrounding mantle would further advance knowledge of lunar mantle hybridization processes.

Summary and conclusions

The last epoch of lunar magma ocean crystallization would produce Fe- and Ti–rich cumulates that contain dense Fe-Ti oxide phases (i.e., IBC). Fe-Ti oxide formation would make the density of these late crystallizing cumulates greater than underlying early crystallizing mafic (olivine and orthopyroxene-rich) cumulates. This gravitationally unstable density contrast would eventually result in a cumulate overturn event where the overlying IBC would sink through the early crystallizing cumulates. We experimentally investigated the chemical reactions that occur during the cumulate overturn process as downwelling IBC melts and mushes interact with early crystallizing mafic (dunite) cumulates.

Experiments run under near solidus conditions reveal that metamorphic transitions in the downwelling IBC would stabilize garnet in the IBC at pressures around 2 GPa during cumulate mantle overturn events. Near solidus experiments demonstrate solid-state diffusive exchange between the IBC material and dunite. Experiments run under supersolidus conditions demonstrate a dissolution–precipitation reaction involving dissolution of dunite and formation of a hybridized melt ± clinopyroxene, depending on the experimental conditions. In the lunar interior, similar chemical reactions may govern the mantle hybridization process. The rate of dunite dissolution is dependent on the pressure, temperature, and saturation state of olivine in the hybridizing melt. Simple kinetic models indicate that formation of volumetrically significant hybridized lunar mantle sources over geologically relevant timescales may require some amount of mechanical mixing, in addition to the chemical reaction mechanisms constrained in this study, depending on the scale of downwelling plumes that develop in the Moon's interior during cumulate mantle overturn.

Supplementary Information The online version contains supplementary material available at https://doi.org/10.1007/s00410-024-02134-z.

Acknowledgements We thank A. Patchen at the University of Tennessee for his assistance with EPMA analysis, and Malcolm Rutherford at Brown University who conditioned the IBC starting materials while a conditioning furnace at the University of Tennessee was under development. The manuscript benefited greatly from the comments and suggestions of the editor Othmar Müntener as well as Yanhao Lin and an anonymous reviewer. This work was supported by NASA Solar System Workings award 80NSSC20K0467 to ND.

Data availability All data supporting the article are reported in the main text and/or the electronic supplement.

References

Anovitz LM, Treiman AH, Essene EJ et al (1985) The heat-capacity of ilmenite and phase equilibria in the system Fe-T-O. Geochim

Cosmochim Acta 49:2027–2040. https://doi.org/10.1016/0016-7037(85)90061-4
Azough F, Freer R (2000) Iron diffusion in single-crystal diopside. Phys Chem Miner 27:732–740. https://doi.org/10.1007/s002690000119
Barr JA, Grove TL (2013) Experimental petrology of the Apollo 15 group a green glasses: melting primordial lunar mantle and magma ocean cumulate assimilation. Geochim Cosmochim Acta 106:216–230. https://doi.org/10.1016/j.gca.2012.12.035
Beard BL, Taylor LA, Scherer EE et al (1998) The source region and melting mineralogy of high-titanium and low-titanium lunar basalts deduced from Lu-Hf isotope data. Geochim Cosmochim Acta 62:525–544. https://doi.org/10.1016/S0016-7037(97)00373-6
Beck AR, Morgan ZT, Liang Y, Hess PC (2006) Dunite channels as viable pathways for mare basalt transport in the deep lunar mantle. Geophys Res Lett. https://doi.org/10.1029/2005GL024008
Borg LE, Carlson RW (2023) The Evolving chronology of moon formation. Annu Rev Earth Planet Sci 51:25–52. https://doi.org/10.1146/annurev-earth-031621-060538
Borg LE, Gaffney AM, Kruijer TS et al (2019) Isotopic evidence for a young lunar magma ocean. Earth Planet Sci Lett 523:115706. https://doi.org/10.1016/j.epsl.2019.07.008
Borinski SA, Hoppe U, Chakraborty S et al (2012) Multicomponent diffusion in garnets I: general theoretical considerations and experimental data for Fe–Mg systems. Contrib Miner Petrol 164:571–586. https://doi.org/10.1007/s00410-012-0758-0
Bottinga Y, Weill DF (1970) Densities of liquid silicate systems calculated from partial molar volumes of oxide components. Amer J Sci 269:169–182. https://doi.org/10.2475/ajs.269.2.169
Brady JB, McCallister RH (1983) Diffusion data for clinopyroxenes from homogenization and self-diffusion experiments. Am Miner 68:95–105
Brown SM, Grove TL (2015) Origin of the Apollo 14, 15, and 17 yellow ultramafic glasses by mixing of deep cumulate remelts. Geochim Cosmochim Acta 171:201–215. https://doi.org/10.1016/j.gca.2015.09.001
Buening DK, Buseck PR (1973) Fe-Mg lattice diffusion in olivine. J Geophys Res 1896–1977(78):6852–6862. https://doi.org/10.1029/JB078i029p06852
Canil D, Bellis AJ (2008) Phase equilibria in a volatile-free kimberlite at 0.1 MPa and the search for primary kimberlite magma. Lithos 105:111–117. https://doi.org/10.1016/j.lithos.2008.02.011
Chakraborty S (1997) Rates and mechanisms of Fe-Mg interdiffusion in olivine at 980°–1300°C. J Geophys Res Solid Earth 102:12317–12331. https://doi.org/10.1029/97JB00208
Chakraborty S, Farver JR, Yund RA, Rubie DC (1994) Mg tracer diffusion in synthetic forsterite and San Carlos olivine as a function of P, T and fO2. Phys Chem Miner 21:489–500. https://doi.org/10.1007/BF00203923
Chakraborty S, Ganguly J (1992) Cation diffusion in aluminosilicate garnets: experimental determination in spessartine-almandine diffusion couples, evaluation of effective binary diffusion coefficients, and applications. Contrib Miner Petrol 111:74–86. https://doi.org/10.1007/BF00296579
Chakraborty S, Rubie DC (1996) Mg tracer diffusion in aluminosilicate garnets at 750–850° C, 1 atm. and 1300° C, 8.5 GPa. Contrib Miner Petrol 122:406–414. https://doi.org/10.1007/s004100050136
Charlier B, Grove TL, Namur O, Holtz F (2018) Crystallization of the lunar magma ocean and the primordial mantle-crust differentiation of the Moon. Geochim Cosmochim Acta 234:50–69. https://doi.org/10.1016/j.gca.2018.05.006
Cohen LH, Ito K, Kennedy GC (1967) Melting and phase relations in an anhydrous basalt to 40 kilobars. Am J Sci 265:475. https://doi.org/10.2475/ajs.265.6.475
Dannberg J, Eilon Z, Faul U et al (2017) The importance of grain size to mantle dynamics and seismological observations. Geochem Geophys Geosyst 18:3034–3061. https://doi.org/10.1002/2017GC006944
Deines P (1974) Temperature-oxygen fugacity tables for selected gas mixtures in the system C–H–O at one atmosphere total pressure. College of Earth and Mineral Sciences, Pennsylvania State University, University Park
Delano JW (1980) Chemistry and liquidus phase relations of Apollo 15 red glass: implications for the deep lunar interior. Lunar Planet Sci Conf Proc 1:251–288
Delano JW (1986) Pristine lunar glasses: criteria, data, and implications. J Geophys Res Solid Earth 91:201–213. https://doi.org/10.1029/JB091iB04p0D201
Dimanov A, Wiedenbeck M (2006) (Fe, Mn)-Mg interdiffusion in natural diopside: effect of pO2. Eur J Mineral 18:705–718. https://doi.org/10.1127/0935-1221/2006/0018-0705
Dohmen R, Chakraborty S (2007) Fe–Mg diffusion in olivine II: point defect chemistry, change of diffusion mechanisms and a model for calculation of diffusion coefficients in natural olivine. Phys Chem Miner 34:409–430. https://doi.org/10.1007/s00269-007-0158-6
Draper DS, duFrane SA, Shearer CK et al (2006) High-pressure phase equilibria and element partitioning experiments on Apollo 15 green C picritic glass: implications for the role of garnet in the deep lunar interior. Geochim Cosmochim Acta 70:2400–2416. https://doi.org/10.1016/j.gca.2006.01.027
Dygert N, Bernard RE, Behr WM (2019) Great basin mantle xenoliths record active lithospheric downwelling beneath central Nevada. Geochem Geophys Geosyst 20:751–772
Dygert N, Hirth G, Liang Y (2016) A flow law for ilmenite in dislocation creep: Implications for lunar cumulate mantle overturn. Geophys Res Lett 43:532–540. https://doi.org/10.1002/2015GL066546
Dygert N, Liang Y, Hess P (2013) The importance of melt TiO2 in affecting major and trace element partitioning between Fe–Ti oxides and lunar picritic glass melts. Geochim Cosmochim Acta 106:134–151. https://doi.org/10.1016/j.gca.2012.12.005
Dygert N, Liang Y, Sun C, Hess P (2014) An experimental study of trace element partitioning between augite and Fe-rich basalts. Geochim Cosmochim Acta 132:170–186. https://doi.org/10.1016/j.gca.2014.01.042
Dygert N, Lin J-F, Marshall EW et al (2017) A low viscosity lunar magma ocean forms a stratified anorthitic flotation crust with mafic poor and rich units. Geophys Res Lett. https://doi.org/10.1002/2017GL075703
Elardo SM, Draper DS, Shearer CK (2011) Lunar Magma ocean crystallization revisited: Bulk composition, early cumulate mineralogy, and the source regions of the highlands Mg-suite. Geochim Cosmochim Acta 75:3024–3045. https://doi.org/10.1016/j.gca.2011.02.033
Elkins Tanton LT, Van Orman JA, Hager BH, Grove TL (2002) Re-examination of the lunar magma ocean cumulate overturn hypothesis: melting or mixing is required. Earth Planet Sci Lett 196:239–249. https://doi.org/10.1016/S0012-821X(01)00613-6
Elkins-Tanton LT, Burgess S, Yin Q-Z (2011) The lunar magma ocean: reconciling the solidification process with lunar petrology and geochronology. Earth Planet Sci Lett 304:326–336. https://doi.org/10.1016/j.epsl.2011.02.004
Elkins-Tanton LT, Chatterjee N, Grove TL (2003) Experimental and petrological constraints on lunar differentiation from the Apollo 15 green picritic glasses. Meteorit Planet Sci 38:515–527. https://doi.org/10.1111/j.1945-5100.2003.tb00024.x
Elthon D, Scarfe CM (1984) High-pressure phase equilibria of a high-magnesia basalt and the genesis of primary oceanic basalts. Am Miner 69:1–15

Farver JR, Yund RA, Rubie DC (1994) Magnesium grain boundary diffusion in forsterite aggregates at 1000°–1300°C and 0.1 MPa to 10 GPa. J Geophys Res Solid Earth 99:19809–19819. https://doi.org/10.1029/94JB01250

Friel JJ, Harker RI, Ulmer GC (1977) Armalcolite stability as a function of pressure and oxygen fugacity. Geochim Cosmochim Acta 41:403–410. https://doi.org/10.1016/0016-7037(77)90268-X

Fujino K (1990) Direct determination of cation diffusion coefficients in pyroxene. Eos 71:943

Ganguly J, Cheng W, Chakraborty S (1998) Cation diffusion in aluminosilicate garnets: experimental determination in pyrope-almandine diffusion couples. Contrib Miner Petrol 131:171–180. https://doi.org/10.1007/s004100050386

Giguere TA, Taylor GJ, Hawke BR, Lucey PG (2000) The titanium contents of lunar mare basalts. Meteorit Planet Sci 35:193–200. https://doi.org/10.1111/j.1945-5100.2000.tb01985.x

Grove TL, Krawczynski MJ (2009) Lunar mare volcanism: where did the magmas come from? Elements 5:29–34. https://doi.org/10.2113/gselements.5.1.29

Haggerty SE (1973) Armalcolite and genetically associated opaque minerals in the lunar samples. Lunar Planet Sci Conf Proc 4:777

Haggerty SE, Lindsley DH (1970) Stability of the pseudobrookite (Fe2TiO5)-ferropseudobrookite (FeTi2O5) series. Carnegie Inst Washington Year Book 68:247–249

Haskin LA, Warren PH (1991) Lunar chemistry. In: lunar sourcebook. pp 357–474

Hess PC, Parmentier EM (1995) A model for the thermal and chemical evolution of the Moon's interior: implications for the onset of mare volcanism. Earth Planet Sci Lett 134:501–514. https://doi.org/10.1016/0012-821X(95)00138-3

Hubbard NJ, Minear JW (1975) A physical and chemical model of early lunar history. In: lunar and planetary science conference proceedings. pp 1057–1085

Hughes SS, Delano JW, Schmitt RA (1990) Chemistry of individual mare volcanic glasses: evidence for distinct regions of hybridized mantle and a KREEP component in Apollo 14 magmatic sources. Lunar Planet Sci Conf Proc 20:127–138

Ito K, Kennedy GC (1971) An experimental study of the basalt-garnet granulite-eclogite transition. In: the structure and physical properties of the earth's crust. pp 303–314

Ji D, Dygert N (2024) Trace element partitioning between apatite and silicate melts: effects of major element composition, temperature, and oxygen fugacity, and implications for the volatile element budget of the lunar magma ocean. Geochim Cosmochim Acta. 369:141–159. https://doi.org/10.1016/j.gca.2023.11.004

Jing J-J, Lin Y, Knibbe JS, van Westrenen W (2022) Garnet stability in the deep lunar mantle: constraints on the physics and chemistry of the interior of the Moon. Earth Planet Sci Lett 584:117491. https://doi.org/10.1016/j.epsl.2022.117491

Jurewicz AJG, Watson EB (1988) Cations in olivine, part 2: diffusion in olivine xenocrysts, with applications to petrology and mineral physics. Contrib Miner Petrol 99:186–201. https://doi.org/10.1007/BF00371460

Kerr RC (1995) Convective crystal dissolution. Contrib Miner Petrol 121:237–246. https://doi.org/10.1007/BF02688239

Kraettli G, Schmidt MW, Liebske C (2022) Fractional crystallization of a basal lunar magma ocean: a dense melt-bearing garnetite layer above the core? Icarus 371:114699. https://doi.org/10.1016/j.icarus.2021.114699

Krawczynski MJ, Grove TL (2012) Experimental investigation of the influence of oxygen fugacity on the source depths for high titanium lunar ultramafic magmas. Geochim Cosmochim Acta 79:1–19. https://doi.org/10.1016/j.gca.2011.10.043

Kress VC, Carmichael ISE (1991) The compressibility of silicate liquids containing Fe2O3 and the effect of composition, temperature, oxygen fugacity and pressure on their redox states. Contrib Miner Petrol 108:82–92. https://doi.org/10.1007/BF00307328

Lange RA, Carmichael ISE (1987) Densities of Na2O-K2O-CaO-MgO-FeO-Fe2O3-Al2O3-TiO2-SiO2 liquids: new measurements and derived partial molar properties. Geochim Cosmochim Acta 51:2931–2946. https://doi.org/10.1016/0016-7037(87)90368-1

Li B, Ge J, Zhang B (2018) Diffusion in garnet: a review. Acta Geochimica 37:19–31. https://doi.org/10.1007/s11631-017-0187-x

Li H, Zhang N, Liang Y et al (2019) Lunar cumulate mantle overturn: a model constrained by ilmenite rheology. J Geophys Res Planets 124:1357–1378. https://doi.org/10.1029/2018JE005905

Liang Y (2000) Dissolution in molten silicates: effects of solid solution. Geochim Cosmochim Acta 64:1617–1627. https://doi.org/10.1016/S0016-7037(00)00331-8

Liang Y (2010) Multicomponent diffusion in molten silicates: theory, experiments, and geological applications. Rev Mineral Geochem 72:409–446. https://doi.org/10.2138/rmg.2010.72.9

Lin Y, Tronche EJ, Steenstra ES, van Westrenen W (2016) Solidification evolution of a dry lunar Magma ocean. Constraint Exp Petrol 47:1296

Lin Y, Tronche EJ, Steenstra ES, van Westrenen W (2017) Evidence for an early wet Moon from experimental crystallization of the lunar magma ocean. Nat Geosci 10:14–18. https://doi.org/10.1038/ngeo2845

Longhi J (1982) Multicomponent phase diagrams and the phase equilibria of basalts. In: magmatic processes of early planetary crusts: Magma oceans and stratiform layered intrusions. p 90

Longhi J (1991) Comparative liquidus equilibria of hypersthene-normative basalts at low pressure. Am Miner 76:785–800

Longhi J (2003) A new view of lunar ferroan anorthosites: postmagma ocean petrogenesis. J Geophys Res 108(E9):5083. https://doi.org/10.1029/2002JE001941

Longhi J (2006) Petrogenesis of picritic mare magmas: constraints on the extent of early lunar differentiation. Geochim Cosmochim Acta 70:5919–5934. https://doi.org/10.1016/j.gca.2006.09.023

Longhi J, Ashwal LD (1985) Two-stage models for lunar and terrestrial anorthosites: petrogenesis without a magma ocean. J Geophys Res Solid Earth 90:C571–C584

Longhi J, Walker D, Grove TL et al (1974) The petrology of the Apollo 17 mare basalts. Lunar Planetary Sci Conf Proc 1:447–469

Longhi J, Walker D, Hays JF (1978) The distribution of Fe and Mg between olivine and lunar basaltic liquids. Geochim Cosmochim Acta 42:1545–1558. https://doi.org/10.1016/0016-7037(78)90025-X

Loomis TP, Ganguly J, Elphick SC (1985) Experimental determination of cation diffusivities in aluminosilicate garnets. Contrib Miner Petrol 90:45–51. https://doi.org/10.1007/BF00373040

Lucey PG, Taylor GJ, Hawke BR, Spudis PD (1998) FeO and TiO2 concentrations in the South Pole-Aitken basin: implications for mantle composition and basin formation. J Geophys Res Planets 103:3701–3708. https://doi.org/10.1029/97JE03146

Mallik A, Ejaz T, Shcheka S, Garapic G (2019) A petrologic study on the effect of mantle overturn: implications for evolution of the lunar interior. Geochim Cosmochim Acta 250:238–250. https://doi.org/10.1016/j.gca.2019.02.014

Maurice M, Tosi N, Hüttig C (2024) Small-scale overturn of high-Ti cumulates promoted by the long lifetime of the lunar magma ocean. J Geophys Res Planets 129:e2023JE008060. https://doi.org/10.1029/2023JE008060

Maurice M, Tosi N, Schwinger S et al (2020) A long-lived magma ocean on a young Moon. Sci Adv. https://doi.org/10.1126/sciadv.aba8949

Morgan Z, Liang Y (2003) An experimental and numerical study of the kinetics of harzburgite reactive dissolution with applications to

dunite dike formation. Earth Planet Sci Lett 214:59–74. https://doi.org/10.1016/S0012-821X(03)00375-3
Morgan Z, Liang Y (2005) An experimental study of the kinetics of lherzolite reactive dissolution with applications to melt channel formation. Contrib Miner Petrol 150:369–385. https://doi.org/10.1007/s00410-005-0033-8
Morgan Z, Liang Y, Hess P (2006) An experimental study of anorthosite dissolution in lunar picritic magmas: implications for crustal assimilation processes. Geochim Cosmochim Acta 70:3477–3491. https://doi.org/10.1016/j.gca.2006.04.027
Müller T, Dohmen R, Becker HW et al (2013) Fe–Mg interdiffusion rates in clinopyroxene: experimental data and implications for Fe–Mg exchange geothermometers. Contrib Miner Petrol 166:1563–1576. https://doi.org/10.1007/s00410-013-0941-y
Nagy KL, Lasaga AC (1992) Dissolution and precipitation kinetics of gibbsite at 80°C and pH 3: the dependence on solution saturation state. Geochim Cosmochim Acta 56:3093–3111. https://doi.org/10.1016/0016-7037(92)90291-P
Nakamura A, Schmalzried H (1984) On the Fe2+ –Mg2+-interdiffusion in olivine (II). Ber Bunsenges Phys Chem 88:140–145. https://doi.org/10.1002/bbpc.19840880212
Neal CR (2001) Interior of the moon: the presence of garnet in the primitive deep lunar mantle. Journal of Geophysical Research: Planets 106:27865–27885. https://doi.org/10.1029/2000JE001386
Nicholis MG, Rutherford MJ (2009) Graphite oxidation in the Apollo 17 orange glass magma: Implications for the generation of a lunar volcanic gas phase. Geochim Cosmochim Acta 73:5905–5917. https://doi.org/10.1016/j.gca.2009.06.022
Paces JB, Nakai S, Neal CR et al (1991) A strontium and neodymium isotopic study of Apollo 17 high-Ti mare basalts: resolution of ages, evolution of magmas, and origins of source heterogeneities. Geochim Cosmochim Acta 55:2025–2043. https://doi.org/10.1016/0016-7037(91)90040-C
Papike JJ, Ryder G, Shearer CK (1998) Lunar samples. Rev Mineral Geochem 36:5–01
Pec M, Holtzman BK, Zimmerman ME, Kohlstedt DL (2020) Influence of lithology on reactive melt flow channelization. Geochem Geophys Geosyst 21:e2020GC008937. https://doi.org/10.1029/2020GC008937
Perchuk AL, Burchard M, Schertl H-P et al (2009) Diffusion of divalent cations in garnet: multi-couple experiments. Contrib Miner Petrol 157:573–592. https://doi.org/10.1007/s00410-008-0353-6
Petry C, Chakraborty S, Palme H (2004) Experimental determination of Ni diffusion coefficients in olivine and their dependence on temperature, composition, oxygen fugacity, and crystallographic orientation. Geochim Cosmochim Acta 68:4179–4188. https://doi.org/10.1016/j.gca.2004.02.024
Rapp JF, Draper DS (2018) Fractional crystallization of the lunar magma ocean: updating the dominant paradigm. Meteorit Planet Sci 53:1432–1455. https://doi.org/10.1111/maps.13086
Ringwood AE, Kesson SE (1976) A dynamic model for mare basalt petrogenesis. In: lunar and planetary science conference proceedings. pp 1697–1722
Roeder PL, Emslie RF (1970) Olivine-liquid equilibrium. Contrib Miner Petrol 29:275–289. https://doi.org/10.1007/BF00371276
Sato M (1979) The driving mechanism of lunar pyroclastic eruptions inferred from the oxygen fugacity behaviour of Apollo 17 orange glass. Lunar and Planetary Science Conference Proceedings 1:311–325
Schmidt MW, Kraettli G (2022) Experimental crystallization of the lunar magma ocean, initial selenotherm and density stratification, and implications for crust formation, overturn and the bulk silicate moon composition. Journal of Geophysical Research: Planets 127:e2022JE007187. https://doi.org/10.1029/2022JE007187
Shearer CK, Elardo SM, Petro NE et al (2015) Origin Of The Lunar Highlands Mg-Suite: An Integrated Petrology. Geochem Chronol Remote Sensing Perspect 100:294–325. https://doi.org/10.2138/am-2015-4817
Shearer CK, Papike JJ (1993) Basaltic magmatism on the moon: a perspective from volcanic picritic glass beads. Geochim Cosmochim Acta 57:4785–4812. https://doi.org/10.1016/0016-7037(93)90200-G
Shearer CK, Papike JJ, Galbreath KC, Shimizu N (1991) Exploring the lunar mantle with secondary ion mass spectrometry: a comparison of lunar picritic glass beads from the apollo 14 and apollo 17 sites. Earth Planet Sci Lett 102:134–147. https://doi.org/10.1016/0012-821X(91)90003-Z
Shepherd K, Namur O, Toplis MJ et al (2022) Trace element partitioning between clinopyroxene, magnetite, ilmenite and ferrobasaltic to dacitic magmas: an experimental study on the role of oxygen fugacity and melt composition. Contrib Miner Petrol 177:90. https://doi.org/10.1007/s00410-022-01957-y
Singletary S, Grove T (2008) Origin of lunar high-titanium ultramafic glasses: a hybridized source? Earth Planet Sci Lett 268:182–189. https://doi.org/10.1016/j.epsl.2008.01.019
Snyder GA, Taylor LA, Neal CR (1992) Combined equilibrium and fractional crystallization of a magma ocean and formation of the upper mantle of the Moon. In: lunar and planetary science conference
Solomon SC, Longhi J (1977) Magma oceanography. I-Thermal evolution. In: Lunar and planetary science conference proceedings. pp 583–599
Springer W, Seck HA (1997) Partial fusion of basic granulites at 5 to 15 kbar: implications for the origin of TTG magmas. Contrib Miner Petrol 127:30–45. https://doi.org/10.1007/s004100050263
Sprung P, Kleine T, Scherer EE (2013) Isotopic evidence for chondritic Lu/Hf and Sm/Nd of the Moon. Earth Planet Sci Lett 380:77–87. https://doi.org/10.1016/j.epsl.2013.08.018
Stolper E, Walker D (1980) Melt density and the average composition of basalt. Contrib Miner Petrol 74:7–12. https://doi.org/10.1007/BF00375484
Sun C, Liang Y (2015) A REE-in-garnet–clinopyroxene thermobarometer for eclogites, granulites and garnet peridotites. Chem Geol 393–394:79–92. https://doi.org/10.1016/j.chemgeo.2014.11.014
Taylor SR (1982) Planetary science: a lunar perspective. Lunar and Planetary Institute, Houston
Taylor AS, Blum JD, Lasaga AC (2000) The dependence of labradorite dissolution and Sr isotope release rates on solution saturation state. Geochim Cosmochim Acta 64:2389–2400. https://doi.org/10.1016/S0016-7037(00)00361-6
Taylor GJ, Wieczorek MA (2014) Lunar bulk chemical composition: a post-gravity recovery and interior laboratory reassessment. Philos Trans Royal Soc Math Phys Eng Sci 372:20130242. https://doi.org/10.1098/rsta.2013.0242
Thacker C, Liang Y, Peng Q, Hess P (2009) The stability and major element partitioning of ilmenite and armalcolite during lunar cumulate mantle overturn. Geochim Cosmochim Acta 73:820–836. https://doi.org/10.1016/j.gca.2008.10.038
Tokle L, Hirth G, Liang Y et al (2021) The effect of pressure and Mg-content on ilmenite rheology: implications for lunar cumulate mantle overturn. J Geophys Res Planet 126:e2020JE006494. https://doi.org/10.1029/2020JE006494
Unruh DM, Stille P, Patchett PJ, Tatsumoto M (1984) Lu-Hf and Sm-Nd evolution in lunar mare basalts. J Geophys Res Solid Earth 89:B459–B477. https://doi.org/10.1029/JB089iS02p0B459
Van Den Bleeken G, Müntener O, Ulmer P (2010) Reaction processes between tholeiitic melt and residual peridotite in the uppermost mantle: an experimental study at 0·8 GPa. J Petrol 51:153–183. https://doi.org/10.1093/petrology/egp066

van der Laan S, Zhang Y, Kennedy AK, Wyllie PJ (1994) Comparison of element and isotope diffusion of K and Ca in multicomponent silicate melts. Earth Planet Sci Lett 123:155–166. https://doi.org/10.1016/0012-821X(94)90264-X

Van der Wal D, Chopra P, Drury M, Gerald JF (1993) Relationships between dynamically recrystallized grain size and deformation conditions in experimentally deformed olivine rocks. Geophys Res Lett 20:1479–1482. https://doi.org/10.1029/93GL01382

Van Orman JA, Grove TL (2000) Origin of lunar high-titanium ultramafic glasses: constraints from phase relations and dissolution kinetics of clinopyroxene-ilmenite cumulates. Meteorit Planet Sci 35:783–794. https://doi.org/10.1111/j.1945-5100.2000.tb01462.x

Wagner TP, Grove TL (1997) Experimental constraints on the origin of lunar high-Ti ultramafic glasses. Geochim Cosmochim Acta 61:1315–1327. https://doi.org/10.1016/S0016-7037(96)00387-0

Walker D, Hays JF (1977) Plagioclase flotation and lunar crust formation. Geology 5:425–428. https://doi.org/10.1130/0091-7613(1977)5%3c425:PFALCF%3e2.0.CO;2

Walker D, Longhi J, Stolper E et al (1974) Experimental petrology and origin of titaniferous lunar basalts. In: lunar and planetary science conference. p 814

Wang C, Liang Y, Xu W, Dygert N (2013) Effect of melt composition on basalt and peridotite interaction: laboratory dissolution experiments with applications to mineral compositional variations in mantle xenoliths from the North China Craton. Contrib Miner Petrol 166:1469–1488. https://doi.org/10.1007/s00410-013-0938-6

Watson EB, Baker DR (1991) Chemical diffusion in magmas: an overview of experimental results and geochemical applications. In: Perchuk LL, Kushiro I (eds) Physical chemistry of magmas. Springer, New York, New York, NY, pp 120–151

Watson EB, Sneeringer MA, Ross A (1982) Diffusion of dissolved carbonate in magmas: experimental results and applications. Earth Planet Sci Lett 61:346–358. https://doi.org/10.1016/0012-821X(82)90065-6

Weitz CM, Rutherford MJ, Head JW (1997) Oxidation states and ascent history of the Apollo 17 volcanic beads as inferred from metal-glass equilibria. Geochim Cosmochim Acta 61:2765–2775. https://doi.org/10.1016/S0016-7037(97)00119-1

Wood JA, Dickey JS Jr, Marvin UB, Powell BN (1970) Lunar anorthosites and a geophysical model of the moon. Geochimica et Cosmochimica Acta Supplement 1:965

Wyatt BA (1977) The melting and crystallisation behaviour of a natural clinopyroxene-ilmenite intergrowth. Contrib Miner Petrol 61:1–9. https://doi.org/10.1007/BF00375941

Xirouchakis DM (2007) Pseudobrookite-group oxide solutions and basaltic melts. Lithos 95:1–9. https://doi.org/10.1016/j.lithos.2006.07.009

Xirouchakis D, Hirschmann MM, Simpson JA (2001) The effect of titanium on the silica content and on mineral-liquid partitioning of mantle-equilibrated melts. Geochim Cosmochim Acta 65:2201–2217. https://doi.org/10.1016/S0016-7037(00)00549-4

Xirouchakis D, Smirnov A, Woody K et al (2002) Thermodynamics and stability of pseudobrookite-type MgTi2O5 (karrooite). Am Miner 87:658–667. https://doi.org/10.2138/am-2002-5-608

Yao L, Liang Y (2012) An Experimental Study of the Solidus of a Hybrid Lunar Cumulate Mantle: Implications for the Temperature at the Core-Mantle Boundary of the Moon. In: 43rd Annual Lunar and Planetary Science Conference. p 2258

Zhang N, Ding M, Zhu M-H et al (2022) Lunar compositional asymmetry explained by mantle overturn following the South Pole-Aitken impact. Nat Geosci 15:37–41. https://doi.org/10.1038/s41561-021-00872-4

Zhang N, Dygert N, Liang Y, Parmentier EM (2017) The effect of ilmenite viscosity on the dynamics and evolution of an overturned lunar cumulate mantle. Geophys Res Lett 44:6543–6552. https://doi.org/10.1002/2017GL073702

Zhang X, Ganguly J, Ito M (2010a) Ca–Mg diffusion in diopside: tracer and chemical inter-diffusion coefficients. Contrib Miner Petrol 159:175–186. https://doi.org/10.1007/s00410-009-0422-5

Zhang Y (1993) A modified effective binary diffusion model. J Geophys Res Solid Earth 98:11901–11920. https://doi.org/10.1029/93JB00422

Zhang Y (2009) Geochemical kinetics. Princetion University Press, Princetion

Zhang Y, Ni H, Chen Y (2010b) Diffusion data in silicate Melts. Rev Mineral Geochem 72:311–408. https://doi.org/10.2138/rmg.2010.72.8

Zhang Y, Walker D, Lesher CE (1989) Diffusive crystal dissolution. Contrib Miner Petrol 102:492–513. https://doi.org/10.1007/BF00371090

Zhang Y, Xu Z (2003) Kinetics of convective crystal dissolution and melting, with applications to methane hydrate dissolution and dissociation in seawater. Earth Planet Sci Lett 213:133–148. https://doi.org/10.1016/S0012-821X(03)00297-8

Zhao Y, de Vries J, van den Berg AP et al (2019) The participation of ilmenite-bearing cumulates in lunar mantle overturn. Earth Planet Sci Lett 511:1–11. https://doi.org/10.1016/j.epsl.2019.01.022